

Modeling Excitable Cells with Memristors

Original

Modeling Excitable Cells with Memristors / Maheshwar, S.; Ascoli, A.; Tetzlaff, R.; Rajamani, V.; Budhathoki, R. K.. - In: JOURNAL OF LOW POWER ELECTRONICS AND APPLICATIONS. - ISSN 2079-9268. - ELETTRONICO. - 14:2(2024). [10.3390/jlpea14020031]

Availability:

This version is available at: 11583/2988905 since: 2024-05-22T08:31:37Z

Publisher:

MDPI

Published

DOI:10.3390/jlpea14020031

Terms of use:



This article is made available under terms and conditions as specified in the corresponding bibliographic description in the repository

Publisher copyright

(Article begins on next page)

Article

Modeling Excitable Cells with Memristors

Maheshwar Sah ^{1,2,*}, Alon Ascoli ³, Ronald Tetzlaff ^{4,*}, Vetriveeran Rajamani ⁵ and Ram Kaji Budhathoki ⁶

¹ Department of Electronics and Communication Engineering, Nepal Engineering College, Changunarayan 44801, Nepal

² TJ Maxx Distribution Center, Evansville, IN 47711, USA

³ Department of Electronics and Telecommunications, Politecnico di Torino, 10129 Turin, Italy; alon.ascoli@polito.it

⁴ Faculty of Electrical and Computer Engineering, Institute of Circuits and Systems, Technische Universität Dresden, 01062 Dresden, Germany

⁵ School of Electronics Engineering (SENSE), Vellore Institute of Technology, Vellore 632014, India; vetrieece86@gmail.com

⁶ Department of Electrical and Electronics Engineering, Kathmandu University, Dhulikhel 45210, Nepal; ramkaji@gmail.com

* Correspondence: sahmaheshwar@gmail.com (M.S.); ronald.tetzlaff@tu-dresden.de (R.T.)

Abstract: This paper presents an in-depth analysis of an excitable membrane of a biological system by proposing a novel approach that the cells of the excitable membrane can be modeled as the networks of memristors. We provide compelling evidence from the Chay neuron model that the state-independent mixed ion channel is a nonlinear resistor, while the state-dependent voltage-sensitive potassium ion channel and calcium-sensitive potassium ion channel function as generic memristors from the perspective of electrical circuit theory. The mechanisms that give rise to periodic oscillation, aperiodic (chaotic) oscillation, spikes, and bursting in an excitable cell are also analyzed via a small-signal model, a pole-zero diagram of admittance functions, local activity, the edge of chaos, and the Hopf bifurcation theorem. It is also proved that the zeros of the admittance functions are equivalent to the eigen values of the Jacobian matrix, and the presence of the positive real parts of the eigen values between the two bifurcation points lead to the generation of complicated electrical signals in an excitable membrane. The innovative concepts outlined in this paper pave the way for a deeper understanding of the dynamic behavior of excitable cells, offering potent tools for simulating and exploring the fundamental characteristics of biological neurons.



Citation: Sah, M.; Ascoli, A.; Tetzlaff, R.; Rajamani, V.; Budhathoki, R.K. Modeling Excitable Cells with Memristors. *J. Low Power Electron. Appl.* **2024**, *14*, 31. <https://doi.org/10.3390/jlpea14020031>

Academic Editor: Stefania Perri

Received: 16 March 2024

Revised: 18 May 2024

Accepted: 22 May 2024

Published: 28 May 2024



Copyright: © 2024 by the authors. Licensee MDPI, Basel, Switzerland. This article is an open access article distributed under the terms and conditions of the Creative Commons Attribution (CC BY) license (<https://creativecommons.org/licenses/by/4.0/>).

Keywords: memristor; excitable cell; oscillation; chaos; spikes; bursting; Chay model; small-signal model; pole-zero diagram; local activity; edge of chaos; Hopf bifurcation

1. Introduction

The electrical activities of neurons are characterized by a diverse array of dynamic phenomena, such as action potential, spike, chaos, and bursting. Understanding these qualitative features are essential for unraveling the principles underlying neuronal excitability. The popular Hodgkin-Huxley (HH) model developed in 1952, which consists of membrane voltage, potassium conductance, sodium conductance, and leakage conductance, provides a framework for understanding the propagation of action potential based on the squid giant axon experiments [1]. Recent analysis revealed that the potassium ion channel and sodium ion channel in the HH model, initially interpreted as time-varying conductances, are in fact generic memristors from the perspective of electrical circuit theory [2–5]. The HH model has spurred significant interest in designing electrical circuit models and observing the experimental results in the wide variety of complex systems of the membrane potential, nervous system, barnacle giant muscle fibers, Purkinje fibers, solitary hair cells, auditory periphery, mini-review of neuromorphic architectures and implementation, organic synapses for neuromorphic electronics, and photochromic compounds [6–16]. Similarly, extensive

research has been conducted to observe the varieties of oscillations in pancreatic β -cells inspired by the HH model [17–26]. The mathematical model of an excitable membrane in pancreatic β -cells consist of voltage-sensitive channels that allow Na^+ and Ca^{2+} to enter the cell and voltage-sensitive K^+ channels and voltage-insensitive K^+ channel that allow K^+ ions to leave the cell and activate intracellular calcium ions, respectively [27–29]. Therefore, the outward current carried by K^+ ions pass through the voltage and calcium-sensitive channels, and the inward currents carried by Na^+ and Ca^{2+} ions pass through the voltage-sensitive Na^+ and Ca^{2+} channels. However, the above models consist of complicated nonlinear differential equations associated with membrane voltage. Later, a modified model was presented by Chay [30], assuming the β -cells of the voltage-sensitive Na^+ conductance are almost inactive and the inward current is almost exclusively carried by Ca^{2+} ions through the voltage-sensitive Ca^{2+} channel. Therefore, the assumption of a mixed effective conductance was formulated without affecting the results by expressing the total inward current in terms of a single mixed conductance g_I and the reversal potential E_I of the two functionally independent Na^+ and Ca^{2+} channels. The model consists of three nonlinear differential equations, in contrast to the other complicated models of an excitable membrane of a pancreatic β -cell. Our studies in this paper typically focus on the simplified Chay neuron model of an excitable cell [30].

Understanding the intricacies of excitable membranes in biological systems are complicated and the mechanisms governing the generation of periodic, aperiodic (chaotic), bursting, and the spiking signals in the cells are still subject to under investigation. This paper aims to explore a model that the state-independent voltage-sensitive mixed ion channel g_I functions as a nonlinear resistor, while the state-dependent voltage-sensitive potassium ion-channel $g_{K,V}$ and calcium-sensitive potassium ion-channel $g_{K,Ca}$ function as time-invariant memristors in Chay neuron model of an excitable cell. Additionally, this study seeks to delve into the memristive model of an excitable cell with the goal of gaining deeper insights into the dynamic behavior of excitable cell through analyses of small signal equivalent circuit models, pole-zero diagrams, local activity principle, edge of chaos and Hopf bifurcation theorem.

The paper is organized as follows: We introduce the Chay neuron model and its comparison analyses with the HH, FitzHugh–Nagumo, and Morris–Lecar (ML) models in Section 2. Section 3 describes the pinched hysteresis fingerprints of ion channel memristors. Section 4 presents the direct current (DC) analysis of the memristive Chay neuron model. Section 5 provides the small-signal analysis. Section 6 explores the application of the local activity principle, the edge of chaos theorem, and Hopf bifurcations in memristive Chay neurons. Finally, Section 7 concludes the paper.

2. Chay Neuron Model of an Excitable Cell

Excitable cells are specialized cells in the body and neurons that are capable of generating electrical signals in response to certain stimuli. These cells are crucial for the functioning of various physiological processes, including nerve signaling, muscle contraction, and hormone release. Excitability in these cells are primarily due to the presence of specialized proteins called ion channels in their cell membranes. These ion channels control the movement of ions such as sodium (Na^+), potassium (K^+), calcium (Ca^{2+}), and chloride (Cl^-) across the membrane, leading to changes in the cell's membrane potential and the generation of electrical signals. The study of excitable cells encompasses a wide array of topics, and our primary aim is to present a unified model for both neuronal and secretory excitable membranes based on the Chay neuron model. The Chay neuron model, which focuses on a simplified representation of neuronal and secretory excitable membranes, aims to provide a unified framework for understanding the complex electrical activity observed in excitable cells. This model typically involves just three ordinary differential equations (ODEs) to capture the essential features of an excitable cell membrane. The model consists of (a) mixed ion channel g_I ; (b) state-dependent voltage-sensitive potassium ion channel

$g_{K,V}$; (c) calcium-sensitive potassium ion channel $g_{K,Ca}$; and (d) leakage channels, which are described by the following differential equations:

$$\frac{dV}{dt} = \frac{I - g_I m_\infty^3 h_\infty (V - E_I) - g_{K,V} n^4 (V - E_K) - g_{K,Ca} \frac{Ca}{1+Ca} (V - E_K) - g_L (V - E_L)}{C_m} \quad (1)$$

$$\frac{dn}{dt} = \frac{n_\infty - n}{\tau_n} \quad (2)$$

$$\frac{dCa}{dt} = -\rho \left[m_\infty^3 h_\infty (V - E_{Ca}) + k_{Ca} Ca \right] \quad (3)$$

where

$$n_\infty = \frac{\alpha_n}{\alpha_n + \beta_n}, \alpha_n = \frac{0.01(V + 20)}{1 - e^{-0.1(V+20)}}, \beta_n = 0.125e^{\left(\frac{-(V+30)}{80}\right)} \quad (4)$$

$$m_\infty = \frac{\alpha_m}{\alpha_m + \beta_m}, \alpha_m = \frac{0.1(V + 25)}{1 - e^{-0.1(V+25)}}, \beta_m = 4e^{\left(\frac{-(V+50)}{18}\right)} \quad (5)$$

$$h_\infty = \frac{\alpha_h}{\alpha_h + \beta_h}, \alpha_h = 0.07e^{\left(\frac{-(V+50)}{20}\right)}, \beta_h = \frac{1}{1 + e^{-0.1(V+20)}}, \tau_n = \frac{1}{\lambda_n(\alpha_n + \beta_n)} \quad (6)$$

Figure 1a shows the typical circuit of the Chay model with external current stimulus, denoted as I (The electrical model is not given in the Chay paper [30]. We have designed a typical electrical circuit model following the differential equations of the membrane potential. The symbolic representation of the conductances and potentials are assumed in different notations compared with the original representation. Figure 1a shows an electrical circuit model following the conventional assumption of the HH model). It consists of membrane potential V of capacitance C_m , potentials E_I , E_K , and E_L for mixed Na^+Ca^{2+} ions, K^+ , and leakage ions, respectively. The conductances g_I , $g_{K,V}$, $g_{K,Ca}$, and g_L represent the voltage-sensitive mixed ion channel, voltage-sensitive potassium ion channel, calcium-sensitive potassium ion channel, and leakage channel, respectively. In the upcoming session, we will provide rigorous proofs that the state-independent mixed ion channel functions as a nonlinear resistor. However, the commonly held belief regarding state-dependent ion channels exhibiting time-varying conductances are found to be conceptually incorrect from the perspective of electrical circuit theory. Contrary to this conventional assumption, these ion channels do not adhere to time-varying conductance principles. Instead, they align more accurately with the characteristics of time-invariant generic memristors from a circuit-theoretic standpoint. A rigorous proof will be demonstrated in the subsequent section. The parameters for this model are summarized in Table 1 (The units of conductance for mixed ion channel, voltage-sensitive potassium ion channel, calcium-sensitive potassium ion channel and leakage ion channel in the Chay model [30] are assumed as $g^* = \frac{\text{conductance}}{\text{membrane capacitance}} = \frac{mS/cm^2}{mF/cm^2} = \frac{1}{\text{second}(s)} = s^{-1}$. As, we are assuming the value of membrane capacitance (C_m) = 1 mF/cm², we use the unit of all the conductances of the ion channels, $g = mS/cm^2$, throughout this study, which is also the equivalent unit g^* of the original Chay model) and a list of abbreviations of the model parameters are illustrated in Appendix A. The comparison analyses of the HH model [1], FitzHugh–Nagumo model [31], ML model [8], and Chay model [30] are summarized in Table 2 along with their respective strengths and limitations. It is notable that each model possesses distinct advantages and drawbacks, making them suitable for different research contexts and questions. The choice of the model depends on the level of detail required, the computational resources available, and the specific phenomena under investigation. This study predominantly centers on the Chay neuron model of excitable cells.

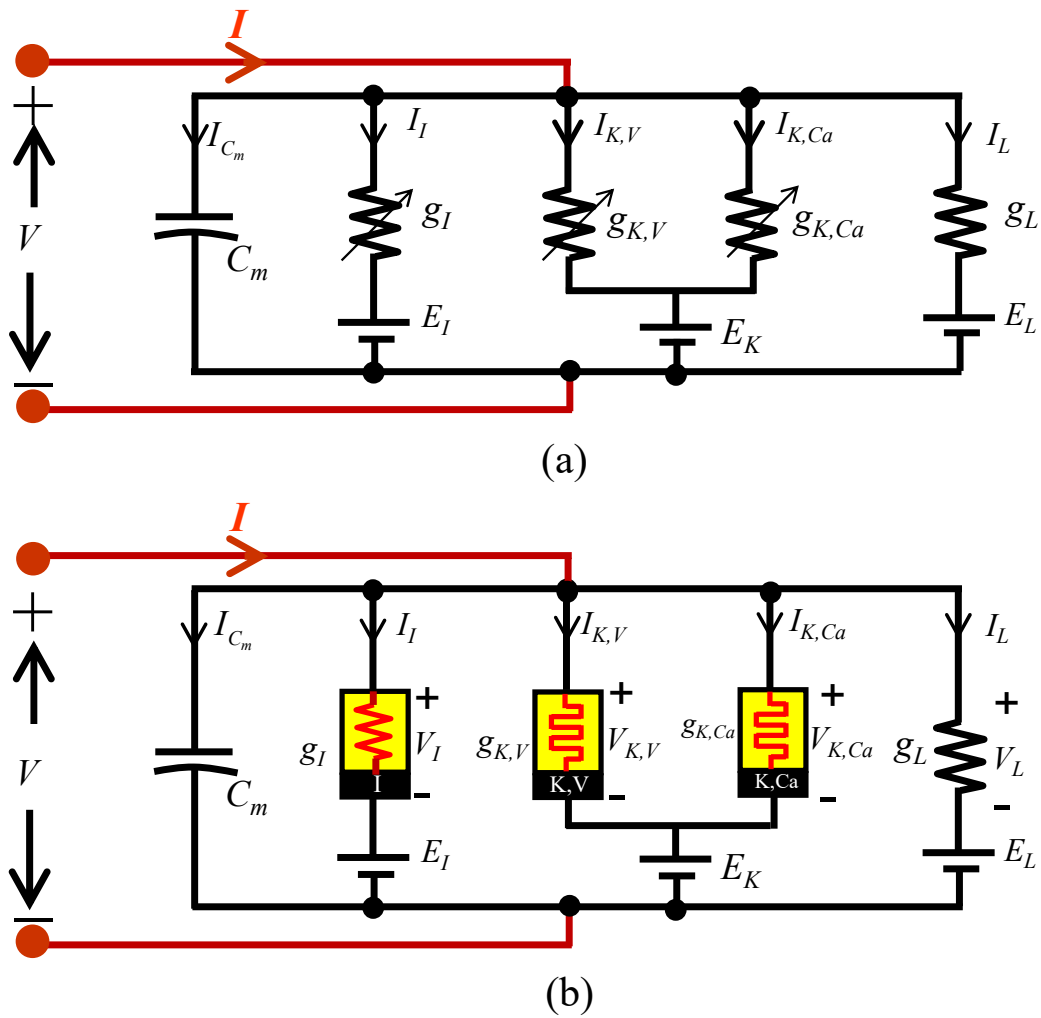


Figure 1. Typical Chay neuron model of an excitable cell [30]. (a) Electrical circuit model, following conventional assumption as time varying conductances [1]. (b) Equivalent memristive Chay model based on Chua’s memristive theory [2–4]. The potential E_{Ca} for Ca^{2+} ion given in the rate of the calcium concentration in Equation (3) is not an external battery source and not shown in external (a) and (b), respectively.

Table 1. Parameters of the Chay neuron model of an excitable cell.

| | | | |
|-------------|----------------------|------------|-------------------------|
| C_m | 1 mF/cm ² | $g_{K,V}$ | 1700 mS/cm ² |
| E_K | −75 mV | g_I | 1800 mS/cm ² |
| E_I | 100 mV | g_L | 7 mS/cm ² |
| E_L | −40 mV | $g_{K,Ca}$ | 10 mS/cm ² |
| E_{Ca} | 100 mV | K_{Ca} | 3.3/18 mV |
| λ_n | 230 | ρ | 0.27 |

Table 2. Comparison analyses of HH, FitzHugh–Nagumo, ML, and Chay models.

| Models | Memristive Models | Strengths | Limitations |
|----------------------|--|--|--|
| HH [1] | The potassium ion channel and sodium ion channel in the HH model are represented by generic memristors [3]. | It is a framework to understand the emergence of action potential propagation in neurons based on the experimental data of the squid giant axon. | It is difficult to generalize to all neurons. Incapable of producing complicated bursting patterns |
| FitzHugh–Nagumo [31] | It does not follow state-dependent Ohm’s law and cannot model with memristors. | Simplified model of neuronal excitation. | Not accurately represent all neuronal behaviors. Incapable of producing bursting |
| ML [8] | It was modeled that the state-independent (dependent) calcium ion channel acts as a nonlinear resistor (generic memristor) and state-dependent potassium ion channel acts as a generic memristor [9,10]. | It is initially presented a model for the barnacle muscle fiber, and later it was considered a popular and simplified representation of the neuron model. | Limited in capturing certain neuronal dynamics. Cannot produce bursting patterns. |
| Chay [30] | We are proposing a framework that the cells of excitable membranes can be modeled as the networks of memristors. | Novel model of excitable cells to capture multiple neuronal states, such as action potentials, periodic oscillations, aperiodic oscillations, spikes, and bursting patterns. | Limited validation in experimental contexts and a lack of details for some applications. |

3. Pinched Hysteresis Fingerprints of the Ion Channel Memristor

A generic memristor driven by a current source or voltage source is a two-terminal electrical circuit element whose instantaneous current or voltage obeys a state-dependent Ohm’s law. A generic memristor driven by a current source can be expressed as follows in terms of state x_n :

$$v = R(x_1, x_2, \dots, x_n)i \tag{7}$$

$$\dot{x}_n = f_1(x_1, x_2, \dots, x_n; i) \tag{8}$$

where $R(x)$ is the memristance of the memristor and depends on “ n ” ($n \geq 1$) state variables.

Similarly, a voltage-controlled memristor is defined in terms of the memductance $G(x)$ and the state variables $x_1, x_2 \dots, x_n$, as follows:

$$i = G(x_1, x_2, \dots, x_n)v \tag{9}$$

$$\dot{x}_n = f_1(x_1, x_2, \dots, x_n; v) \tag{10}$$

Equations (7)–(10) play significant roles in distinguishing the memristive and non-memristive systems [32,33]. They provide evidence that the state independent voltage-sensitive mixed ion channel functions as a nonlinear resistor, and state-dependent voltage-sensitive potassium ion channel and calcium-sensitive potassium ion channel behave as time-invariant generic memristors.

3.1. Voltage-Sensitive Mixed Ion channel Nonlinear Resistor

The time-varying voltage-sensitive mixed ion channel with input voltage v_I and current i_I in the second element (from left) in Figure 1a is given by

$$V - E_I = v_I \tag{11}$$

and

$$i_I = G_I(m_\infty, h_\infty) v_I \tag{12}$$

and the conductance of the voltage-sensitive mixed ion channel is given by

$$G_I(m_\infty, h_\infty) = g_I m_\infty^3 h_\infty \tag{13}$$

where m_∞ and h_∞ are computed using Equations (5) and (6).

$$m_\infty = \frac{0.1(v_I + E_I + 25)}{0.1(v_I + E_I + 25) + 4(1 - e^{-0.1(v_I + E_I + 25)})e^{\left(\frac{-(v_I + E_I + 50)}{18}\right)}} \quad (14)$$

$$h_\infty = \frac{0.07\left(1 + e^{-0.1(v_I + E_I + 20)}\right)e^{\left(\frac{-(v_I + E_I + 50)}{20}\right)}}{0.07\left(1 + e^{-0.1(v_I + E_I + 20)}\right)e^{\left(\frac{-(v_I + E_I + 50)}{20}\right)} + 1} \quad (15)$$

Observe Equations (12)–(15) are not identical to Equations (7) and (8) or Equations (9) and (10) in terms of state dependent Ohm’s law. Consequently, the time-varying voltage-sensitive mixed ion channel can be substituted by a nonlinear resistor (A mixed ion channel is a nonlinear voltage-controlled resistor with conductance $G_I(m_\infty, h_\infty)$, where m_∞ and h_∞ are the functions of the voltage v_I across the two-terminal element.), as depicted in the second element (from the left) in Figure 1b. To verify the voltage-sensitive mixed ion channel is a nonlinear resistor, an extensive numerical simulation for a sinusoidal input voltage source $v_I = 100\sin(2\pi ft)$ mV is performed for the three different frequencies, namely, $f = 100$ Hz, 200 Hz, and 1 KHz, respectively. Figure 2 shows the corresponding output nonlinear waveform on the current i_I vs. voltage v_I plane for these frequencies, confirming that the mixed ion channel exhibits the properties of a nonlinear resistor.

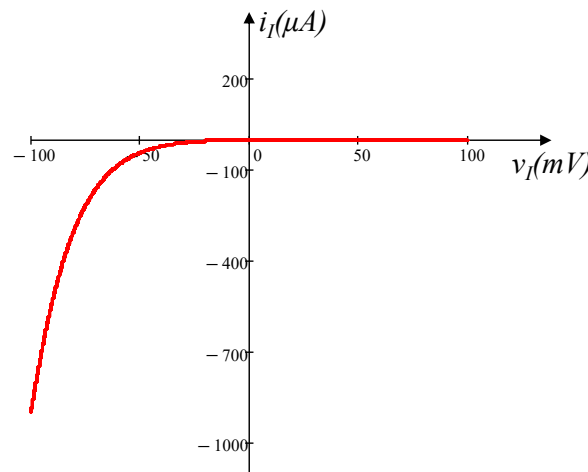


Figure 2. Output waveform plotted on the i_I vs. v_I plane when the input voltage $v_I = 100\sin(2\pi ft)$ mV is applied with three different frequencies, namely $f = 100$ Hz, 200 Hz, and 1 KHz, to the voltage-sensitive mixed ion channel. The output nonlinear waveform observed in Figure 2 for different frequencies confirms the mixed ion channel is a nonlinear resistor.

3.2. Voltage-Sensitive Potassium Ion Channel Memristor

Let us define the voltage across the voltage-sensitive potassium ion channel shown in the third (from left) element in Figure 1a as $v_{K,V}$, and the current is $i_{K,V}$. Then

$$V - E_K = v_{K,V} \quad (16)$$

and the current entering the channel is

$$i_{K,V} = G_{K,v}(n) v_{K,V} \quad (17)$$

where the memductance is given by

$$G_{K,V}(n) = g_{K,V} n^4 \quad (18)$$

and the state equation describing the channel in terms of n can be simplified from Equation (2) as

$$\frac{dn}{dt} = f(n; v_{K,V}) = \lambda_n \left[\frac{0.01(v_{K,V} + E_K + 20)}{1 - e^{-0.1(v_{K,V} + E_K + 20)}} (1 - n) - 0.125 e^{\left(\frac{-(v_{K,V} + E_K + 30)}{80}\right)} n \right] \quad (19)$$

Note that Equations (17)–(19) are identical to the voltage-controlled generic memristor defined in Equations (9)–(10) with a first-order differential equation. Hence, the time-varying conductance shown in Figure 1a of the voltage-sensitive potassium ion channel is replaced with the voltage-sensitive potassium ion channel memristor, as shown in the third element (from left) in Figure 1b.

We observed the memristive fingerprint of the voltage-sensitive potassium ion channel memristor by applying a sinusoidal bipolar signal at different frequencies. This property asserts that beyond some frequency f^* , the pinched hysteresis loops characterized by a memristor shrink to a single-valued function through the origin as frequency $f > f^*$ tends to infinity. To verify this property, a sinusoidal voltage source $v_{K,V}(t) = 100\sin(2\pi ft)$ mV is applied to the voltage-sensitive potassium ion channel with frequencies $f = 100$ KHz, 500 KHz, and 4 MHz, respectively. As shown in Figure 3, the zero-crossing pinched hysteresis loops shrink as the frequencies increase and tend to a straight line at 4 MHz, which confirms that the voltage-sensitive potassium ion channel is a generic memristor. All of these pinched hysteresis loops exhibit the fingerprints of a memristor [33].

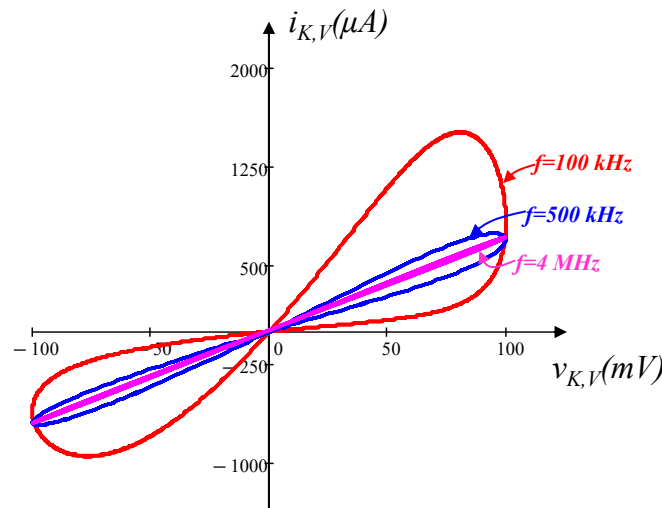


Figure 3. Pinched hysteresis loops of voltage-sensitive potassium ion channel memristor at frequencies $f = 100$ KHz, 500 KHz, and 4 MHz for the input signal $v_{K,V}(t) = 100\sin(2\pi ft)$ mV.

3.3. Calcium-Sensitive Potassium Ion Channel Memristor

Let us consider the input voltage of the calcium-sensitive potassium ion channel. The fourth element (from left) in Figure 1a is $v_{K,Ca}$ (Since the same potential E_K is shared by the voltage-sensitive potassium ion channel memristor and calcium-sensitive potassium ion channel memristor, the voltage assumed, $V - E_K = v_{K,V}$ in Equation (16) and $V - E_K = v_{K,Ca}$ in Equation (21), are identical. The voltages $v_{K,V}$ and $v_{K,Ca}$ are assumed to distinguish the input voltage applied to the voltage-sensitive potassium ion channel memristor and the calcium-sensitive potassium ion channel memristor, respectively.) and the current is $i_{K,Ca}$. The current entering the channel is given by

$$i_{K,Ca} = G_{K,Ca}(Ca)v_{K,Ca} \quad (20)$$

where

$$V - E_K = v_{K,Ca} \quad (21)$$

and the memductance of the calcium-sensitive potassium channel is given by

$$G_{K,Ca}(Ca) = g_{K,Ca} \frac{Ca}{1 + Ca} \tag{22}$$

The state equation in terms of calcium concentration from Equations (3) and (5) is given by

$$\frac{dCa}{dt} = f(Ca; V_{K,Ca}) = -\rho \left[m_{\infty}^3 h_{\infty}(v_{K,Ca} + E_K - E_{Ca}) + k_{Ca} Ca \right] \tag{23}$$

Observe that Equations (20)–(23) are examples of a voltage-controlled memristor defined in Equations (9)–(10) in terms of the calcium concentration channel Ca . Since only one state equation is defined in terms of Ca , we call this memristor a first-order calcium-sensitive potassium ion channel generic memristor. Therefore, the time-varying calcium-sensitive potassium ion channel is replaced with a calcium-sensitive potassium ion channel memristor, as shown in the fourth element (from left) in Figure 1b.

Let us verify the fingerprint of the frequency-dependent pinched hysteresis loops of the calcium-sensitive potassium ion channel by applying the sinusoidal voltage source $v_{KCa}(t) = 100\sin(2\pi ft)$ mV with frequencies $f = 10$ Hz, 30 Hz, and 200 Hz, respectively. Observe from Figure 4 that all the zero-crossing pinched hysteresis loops shrink as the frequencies of the input signal increases and tend to a straight line for the frequency $f = 200$ Hz. All of the pinched hysteresis fingerprints confirm that the calcium-sensitive potassium ion channel is a generic memristor.

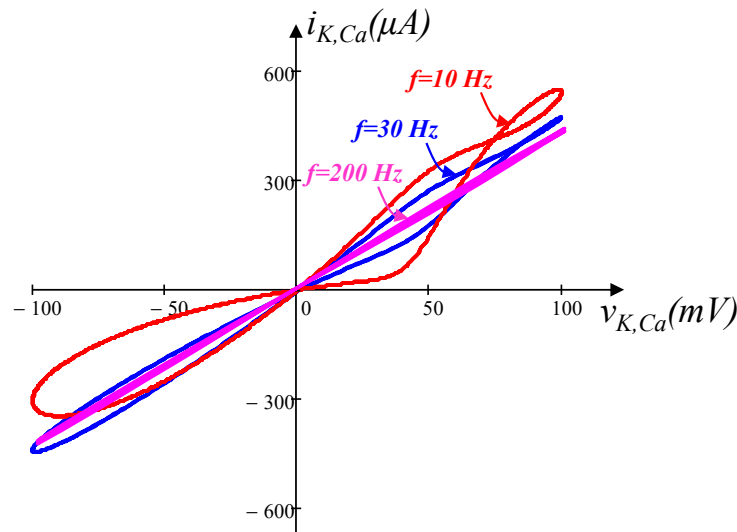


Figure 4. Pinched hysteresis loops of the calcium-sensitive potassium ion channel memristor at frequencies $f = 10$ Hz, 30 Hz, and 200 Hz for the input signal $v_{K,Ca}(t) = 100\sin(2\pi ft)$ mV.

4. DC Analysis of the Memristive Chay Model of an Excitable Cell

The primary objective of analyzing the DC behavior of the memristive Chay model is to identify the equilibrium points of the nonlinear equations. These equilibrium points represent the steady-state solutions obtained by equating the rate of change of equilibrium voltage V_m , gate activation n of the voltage-sensitive potassium ion channel memristor, and concentration of calcium-sensitive Ca of the calcium-sensitive potassium ion channel memristor to zero from Equations (1), (2), and (3), respectively. By determining these equilibrium points, insights can be gained into the behavior of the excitable cell under different conditions, such as varying input stimuli or parameter values, and can be expressed as a function of current I as follows:

$$n = n_{\infty}(V_m) \triangleq \hat{n}(V_m) \tag{24}$$

$$Ca = Ca_{\infty}(V_m) \triangleq \hat{Ca}(V_m) \tag{25}$$

$$I = g_I m_\infty^3 h_\infty (V_m - E_I) + g_{K,V} \hat{n}^4 (V_m - E_K) + g_{K,Ca} \frac{C\hat{a}}{1 + C\hat{a}} (V_m - E_K) + g_L (V_m - E_L) \quad (26)$$

The external current I expressed as the function of membrane voltage V_m in Equation (26) gives the *explicit* formula of the DC V - I curve of the memristive Chay model. We have plotted the individual DC V - I curves of the voltage-sensitive mixed ion channel non-linear resistor, voltage-sensitive potassium ion channel memristor, calcium-sensitive potassium ion channel memristor, and leakage channel at equilibrium voltages V_I , $V_{K,V}$, $V_{K,Ca}$ and V_L , as shown in Figure 5b, Figure 5c, Figure 5d, and Figure 5e, respectively. Figure 5f shows the DC V - I curve of Figure 5a over the range of DC voltage $-50 \text{ mV} < V_m < -24 \text{ mV}$. For any DC value of V_m , we calculated the corresponding value of I as the vertical axis. Our extensive calculations show that the two Hopf bifurcation points occur at $V_m = -48.763 \text{ mV}$ (resp., $I = -66.671 \text{ }\mu\text{A}$) and $V_m = -27.984 \text{ mV}$ (resp., $I = 433.594 \text{ }\mu\text{A}$), respectively. Details of these two bifurcation points will be discussed in upcoming section.

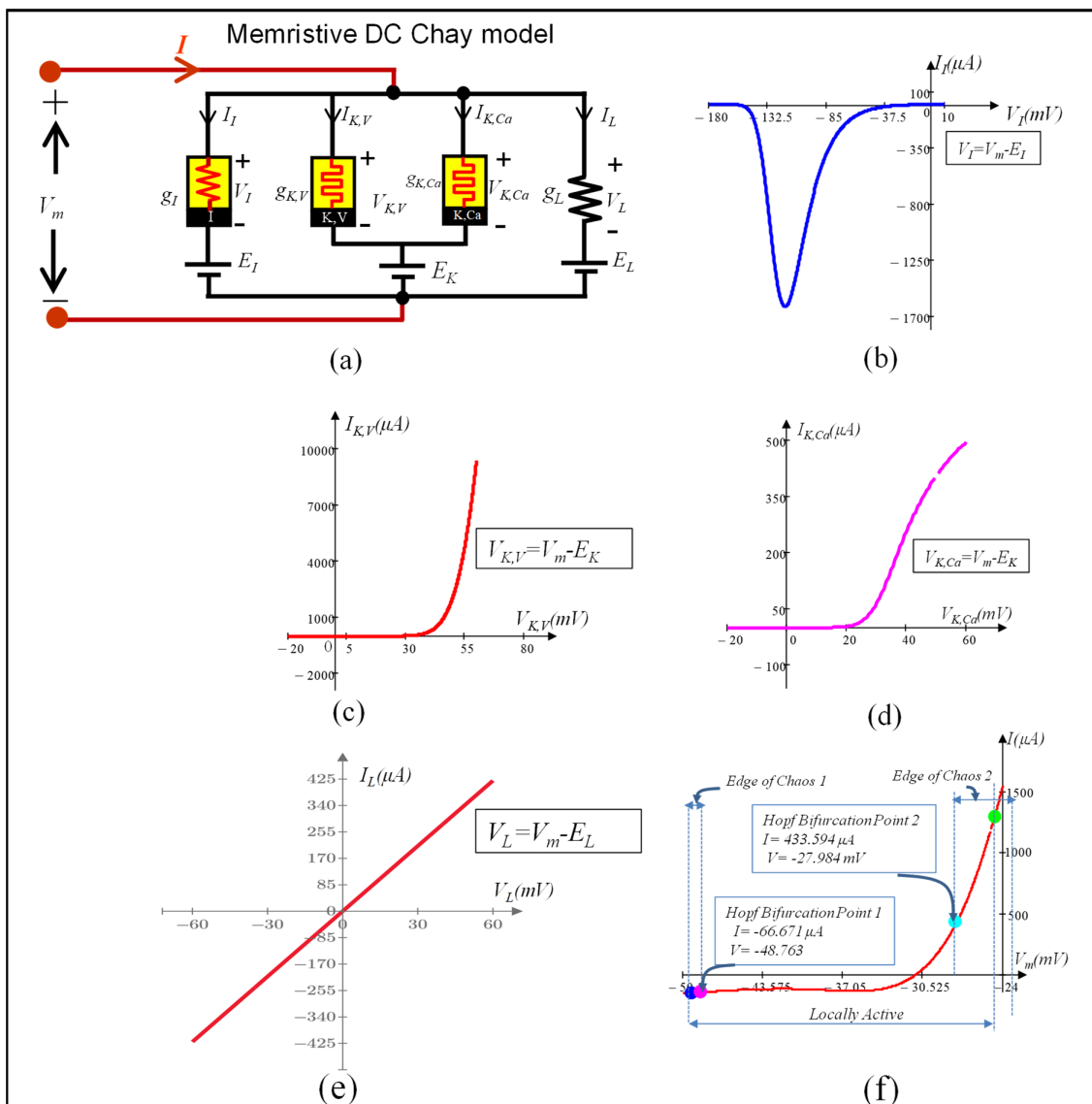


Figure 5. (a) Memristive DC Chay model at equilibrium voltage V_m . (b) DC V - I curve of a mixed ion channel nonlinear resistor at equilibrium voltage $V_I = V_m - E_I$. (c) DC V - I curve of voltage-sensitive potassium ion channel memristor at equilibrium voltage $V_{K,V} = V_m - E_K$. (d) DC V - I curve of the calcium-sensitive potassium ion channel memristor at equilibrium voltage $V_{K,Ca} = V_m - E_K$. (e) DC V - I curve of the leakage channel at equilibrium voltage $V_L = V_m - E_L$. (f) Plot of the DC V - I curve of the memristive Chay model at membrane voltage V_m .

5. Small-Signal Circuit Model

The small-signal equivalent circuit is a linearized method to predict the response of electronic circuits when a small input signal is applied to an equilibrium point Q . The objective of this section is to analyze the small-signal response of a voltage-sensitive mixed ion channel nonlinear resistor, a voltage-sensitive potassium ion channel memristor, and a calcium-sensitive potassium ion channel memristor using Taylor series expansion and Laplace transformation.

5.1. Small-Signal Circuit Model of the Mixed Ion Channel Nonlinear Resistor

The small signal equivalent circuit of the mixed ion channel nonlinear resistor at an equilibrium point Q_I (The equilibrium point Q_I at $v_i = V_I$ is obtained by solving Equation (12)) on the DC V_I - I_I curve is derived as follows:

$$v_I = V_I(Q_I) + \partial v_I \tag{27}$$

$$i_I = I_I(Q_I) + \partial i_I \tag{28}$$

Applying Taylor series expansion to the voltage-sensitive mixed ion channel nonlinear resistor defined in Equations (27) and (28) at the DC operating point Q_I , we get

$$\begin{aligned} i_I &= f(V_I + \delta v_I) = a_{00}(Q_I) + a_{12}(Q_I)\delta v_I + h.o.t. \\ &= I_I(Q_I) + \delta i_I \end{aligned} \tag{29}$$

where *h.o.t* denotes higher-order terms and coefficients can be computed as

$$a_{00}(Q_I) = G_I(Q_I)V_I(Q_I) = I_I(Q_I) \tag{30}$$

$$a_{12}(Q_I) = \frac{\partial f(v_I)}{\partial v_I} \tag{31}$$

Linearize Equation (29) by neglecting the *h.o.t*. then

$$\delta i_I = a_{12}(Q_I)\delta v_I \tag{32}$$

Taking the Laplace transform of Equation (32), we obtain

$$\hat{i}_I(s) = a_{12}(Q_I)\hat{v}_I(s) \tag{33}$$

The admittance $Y_I(s; Q_I)$ of the small-signal equivalent circuit of the voltage-sensitive mixed ion channel nonlinear resistor at the DC operating point Q_I is given by

$$Y_I(s; Q_I) = \frac{\hat{i}_I(s)}{\hat{v}_I(s)} = a_{12}(Q_I) = \frac{1}{\frac{1}{a_{12}(Q_I)}} = \frac{1}{R_{1I}} \tag{34}$$

where

$$R_{1,I} = 1/a_{12}(Q_I) \tag{35}$$

From Equation (34), it is clear that the small-signal admittance function of the *mixed ion channel* nonlinear resistor is equivalent to that of a linear resistor. The corresponding small-signal equivalent circuit and a plot of the coefficients $a_{12}(Q_I)$ and resistance $R_{1,I}$ as a function of the DC equilibrium voltage $V_I = V_m - E_I$, where $E_I = 100$ mV, are shown in Figures 6a and 6b, respectively. The explicit formulas for computing coefficient $a_{12}(Q_I)$ are given in Figure 7 for readers' convenience.

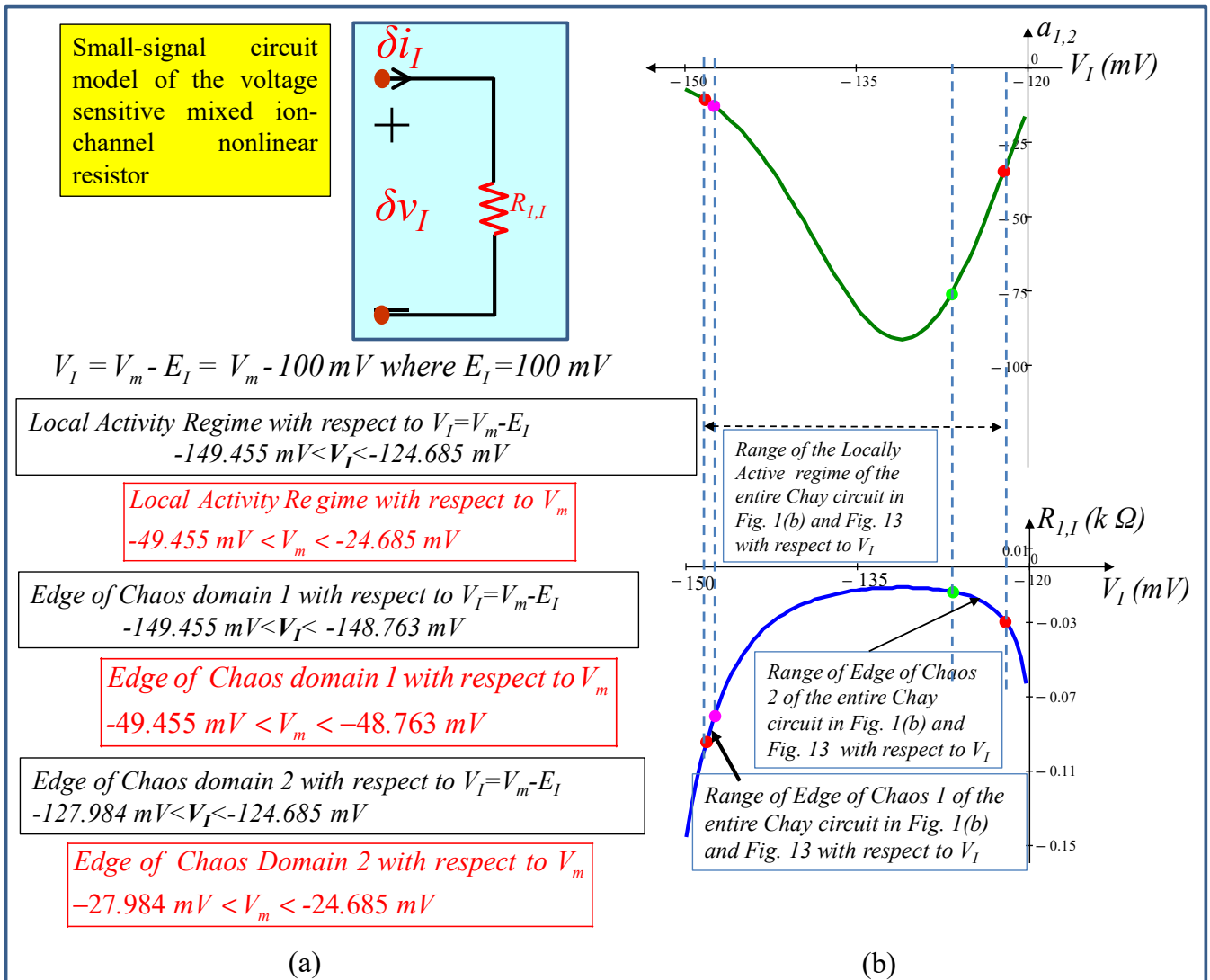


Figure 6. (a) Small-signal circuit model of the voltage-sensitive mixed ion channel nonlinear resistor about the DC equilibrium point $Q_I (V_I, I_I)$. (b) Plot of the coefficient $a_{1,2}$ and resistance $R_{1,I}$ as a function of the DC equilibrium voltage $V_I = V_m - E_I$, where $E_I = 100 \text{ mV}$. $R_{1,I} < 0$ over the range of local activity, edge of chaos 1 and edge of chaos 2 of the mixed ion channel nonlinear resistor is identified with respect to V_I of the entire Chay circuit in Figure 1b and Figure 16.

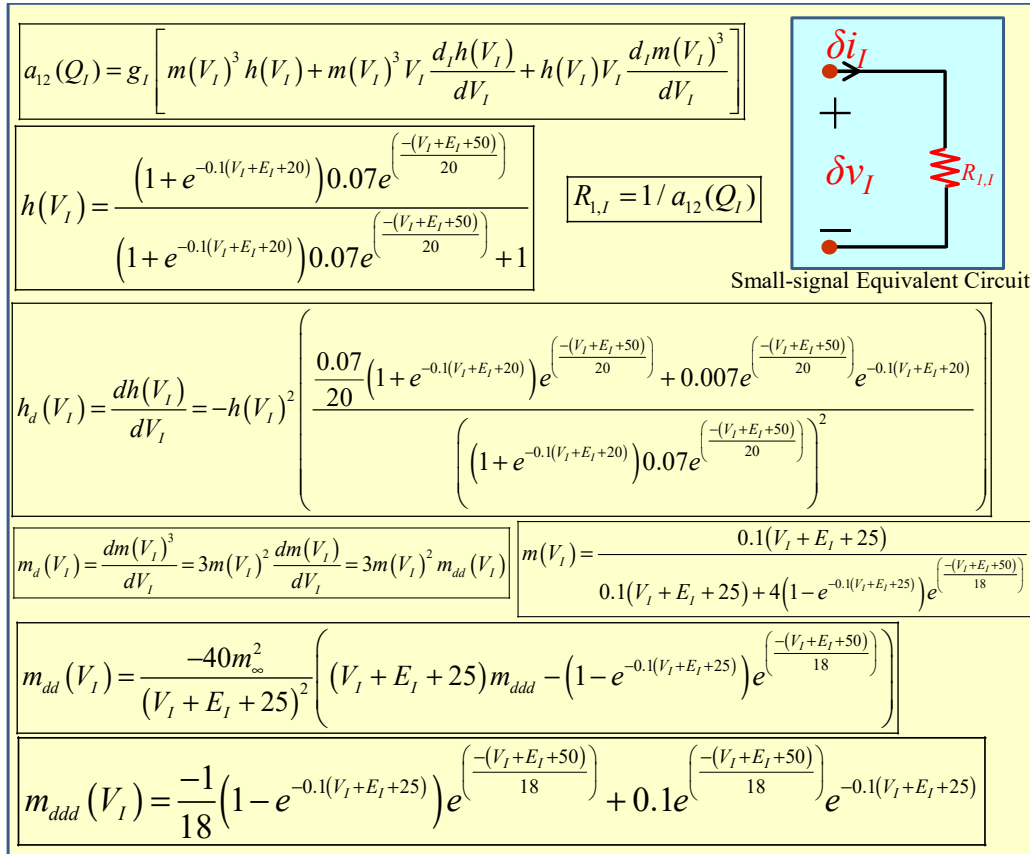


Figure 7. Explicit formulas for computing the coefficients $a_{12}(Q_I)$ of the voltage-sensitive mixed ion channel nonlinear resistor.

5.2. Small-Signal Circuit Model of the Voltage-Sensitive Potassium Ion Channel Memristor

The small-signal circuit model of the voltage-sensitive potassium ion channel memristor at an equilibrium point $Q_{K,V}$ (The equilibrium point $Q_{K,V}$ at $v_{K,V} = V_{K,V}$ is obtained from Equation (19) by solving $f(n; V_{K,V}) = 0$ for $n = n_{K,V}$. The explicit formula for $n(V_{K,V})$ is given in Figure 11) on the DC $V_{K,V}$ - $I_{K,V}$ curve is derived by defining

$$n = n_{Q_{K,V}} + \delta n \tag{36}$$

$$v_{K,V} = V_{K,V}(Q_{K,V}) + \delta v_{K,V} \tag{37}$$

$$i_{K,V} = I_{K,V}(Q_{K,V}) + \delta i_{K,V} \tag{38}$$

Expanding $i_{K,V} = G_{K,V}(n)v_{K,V}$ from Equation (17) in a Taylor series about the equilibrium point $(N(Q_{K,V}), V_{K,V}(Q_{K,V}))$, we obtain

$$\begin{aligned} i_{K,V} &= a_{00}(Q_{K,V}) + a_{11}(Q_{K,V}) \delta n + a_{12}(Q_{K,V}) \delta v_{K,V} + h.o.t. \\ &= I_{K,V}(Q_{K,V}) + \delta i_{K,V} \end{aligned} \tag{39}$$

where

$$\delta n = n - n_{Q_{K,V}} \tag{40}$$

$$\delta v_{K,V} = v_{K,V} - V_{K,V}(Q_{K,V}) \tag{41}$$

$$\delta i_{K,V} = i_{K,V} - I_{K,V}(Q_{K,V}) \tag{42}$$

and

$$a_{00}(Q_{K,V}) = G_{K,V}(Q_{K,V})V_{K,V}(Q_{K,V}) = I_{K,V}(Q_{K,V}) \tag{43}$$

$$a_{11}(Q_{K,V}) = V_{K,V}(Q_{K,V})G'_{K,V}(n_{Q_{K,V}}) \tag{44}$$

$$a_{12}(Q_{K,V}) = G_{K,V}(n_{Q_{K,V}}) \tag{45}$$

and *h.o.t.* denotes the higher-order terms. Let us linearize the nonlinear equation by neglecting the *h.o.t.* in Equation (39), then:

$$\delta i_K = a_{11}(Q_{K,V})\delta n + a_{12}(Q_{K,V})\delta v_{K,V} \tag{46}$$

Similarly, expanding the state equation $f(n_{K,V}, V_{K,V})$ in Equation (19) using a Taylor series about the equilibrium point $(n(Q_{K,V}), V_{K,V}(Q_{K,V}))$, we obtain

$$\begin{aligned} f(n_{Q_{K,V}} + \delta n, V_{K,V}(Q_{K,V}) + \delta v_{K,V}) \\ = f(n_{Q_{K,V}}, V_{K,V}(Q_{K,V})) + b_{11}(Q_{K,V})\delta n + b_{12}(Q_{K,V})\delta v_{K,V} + h.o.t. \end{aligned} \tag{47}$$

where

$$b_{11}(Q_{K,V}) = \left. \frac{\partial f_n(n, v_{K,V})}{\partial n} \right|_{Q_{K,V}} \tag{48}$$

$$b_{12}(Q_{K,V}) = \left. \frac{\partial f_N(n, v_{K,V})}{\partial v_{K,V}} \right|_{Q_{K,V}} \tag{49}$$

Linearizing the nonlinear state Equation (47) by neglecting the *h.o.t.*, we get

$$\frac{d(\delta n)}{dt} = b_{11}(Q_{K,V})\delta n + b_{12}(Q_{K,V})\delta v_{K,V} \tag{50}$$

Taking Laplace transform of Equations (46) and (50), we obtain

$$\hat{i}_{K,V}(s) = a_{11}(Q_{K,V})\hat{n}(s) + a_{12}(Q_{K,V})\hat{v}_{K,V}(s) \tag{51}$$

$$s \hat{n}(s) = b_{11}(Q_{K,V})\hat{n}(s) + b_{12}(Q_{K,V})\hat{v}_{K,V}(s) \tag{52}$$

Solving Equation (52) for $\hat{n}(s)$ and substituting the result into Equation (51), we obtain the following admittance $Y_{K,V}(s; Q_{K,V})$ for the small-signal equivalent circuit of the voltage-sensitive potassium ion channel memristor at equilibrium point $Q_{K,V}$:

$$Y_{K,V}(s; Q_{K,V}) = \frac{\hat{i}_{K,V}(s)}{\hat{v}_{K,V}(s)} = \left[\frac{1}{\frac{s}{a_{11}(Q_{K,V})b_{12}(Q_{K,V})} - \frac{b_{11}(Q_{K,V})}{a_{11}(Q_{K,V})b_{12}(Q_{K,V})}} + \frac{1}{a_{12}(Q_{K,V})} \right] \tag{53}$$

$$Y_{K,V}(s; Q_{K,V}) = \left(\frac{1}{(sL_{K,V} + R_{1K,V})} + \frac{1}{R_{2K,V}} \right) \tag{54}$$

$$\text{where } L_{K,V} \triangleq \frac{1}{a_{11}(Q_{K,V})b_{12}(Q_{K,V})} \tag{55}$$

$$R_{1K,V} \triangleq -\frac{b_{11}(Q_{K,V})}{a_{11}(Q_{K,V})b_{12}(Q_{K,V})} \tag{56}$$

$$R_{2K,V} \triangleq \frac{1}{a_{12}(Q_{K,V})} \tag{57}$$

It follows from Equations (55)–(57) that the small-signal admittance function of the first-order voltage-sensitive potassium ion channel memristor is equivalent to the series connection of an inductor and a resistor in parallel with another resistor, as shown in Figure 8. The corresponding coefficients a_{11} , a_{12} , b_{11} , b_{12} , inductance $L_{K,V}$, resistance $R_{1K,V}$, and resistance $R_{2K,V}$ as a function of the DC equilibrium voltage $V_{K,V} = V_m - E_K$, where $E_K = -75$ mV are shown in Figures 9 and 10, respectively. Please note that the local activity,

edge of chaos 1, and edge of chaos 2, shown in Figure 10a–c, are not the local activity and edge of chaos domains of the separate two terminals of the voltage-sensitive potassium ion channel memristor. The small signal positive inductance and resistances (i.e., $L_{K,V} > 0$, $R_{1K,V} > 0$, and $R_{2K,V} > 0$) of the potassium ion channel memristor observed over the local activity, edge of chaos 1 and edge of chaos 2 regime are just the corresponding range of the voltage with respect to $V_{K,V}$ of the entire connected Chay small-signal equivalent circuit of Figure 1b and Figure 16. For the readers' convenience, the explicit formulas for computing the coefficients $a_{11}(Q_{K,V})$, $a_{12}(Q_{K,V})$, $b_{11}(Q_{K,V})$, $b_{12}(Q_{K,V})$, and $L_{K,V}$, $R_{1K,V}$, and $R_{2K,V}$ are summarized in Figure 11.

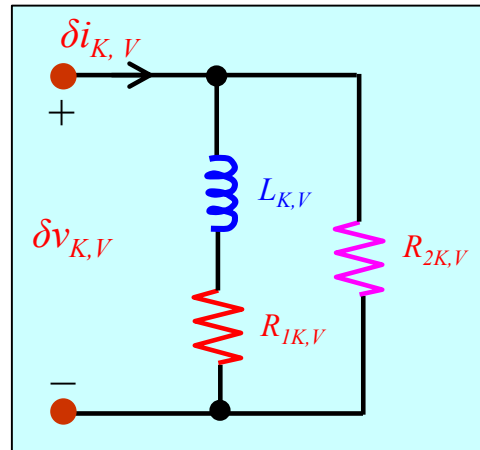


Figure 8. Small-signal equivalent circuit model of the voltage-sensitive potassium ion channel memristor about the DC equilibrium point $Q_{K,V}$ ($V_{K,V}$, $I_{K,V}$).

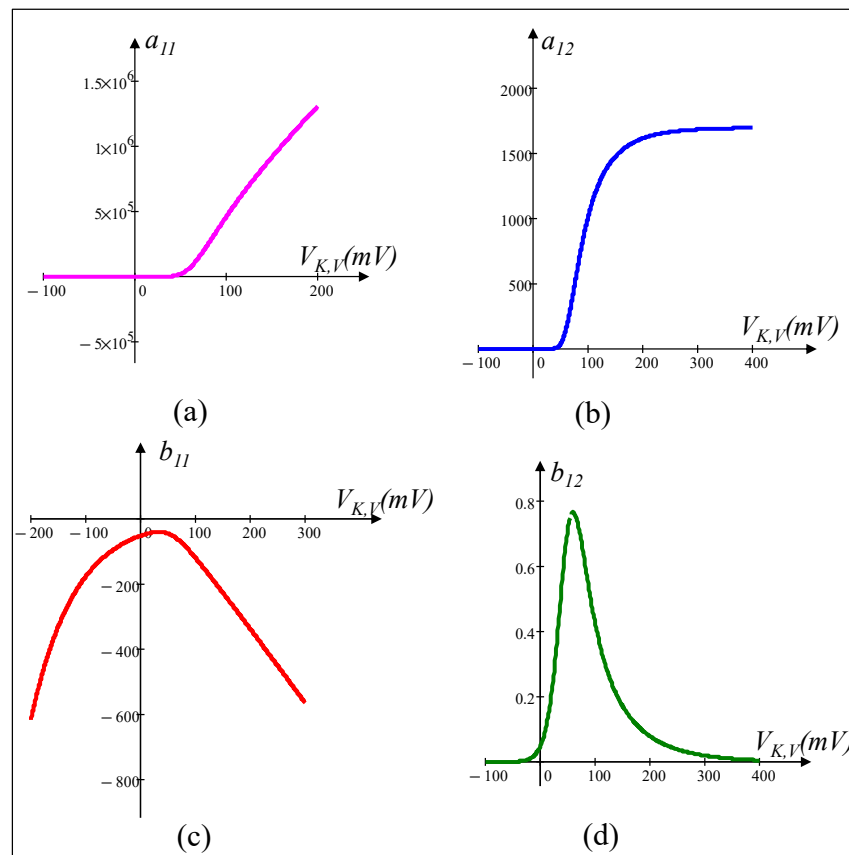


Figure 9. Plot of coefficients (a) a_{11} , (b) a_{12} , (c) b_{11} , and (d) b_{12} of the voltage-sensitive potassium ion channel memristor as a function of the DC equilibrium voltage $V_{K,V}$.

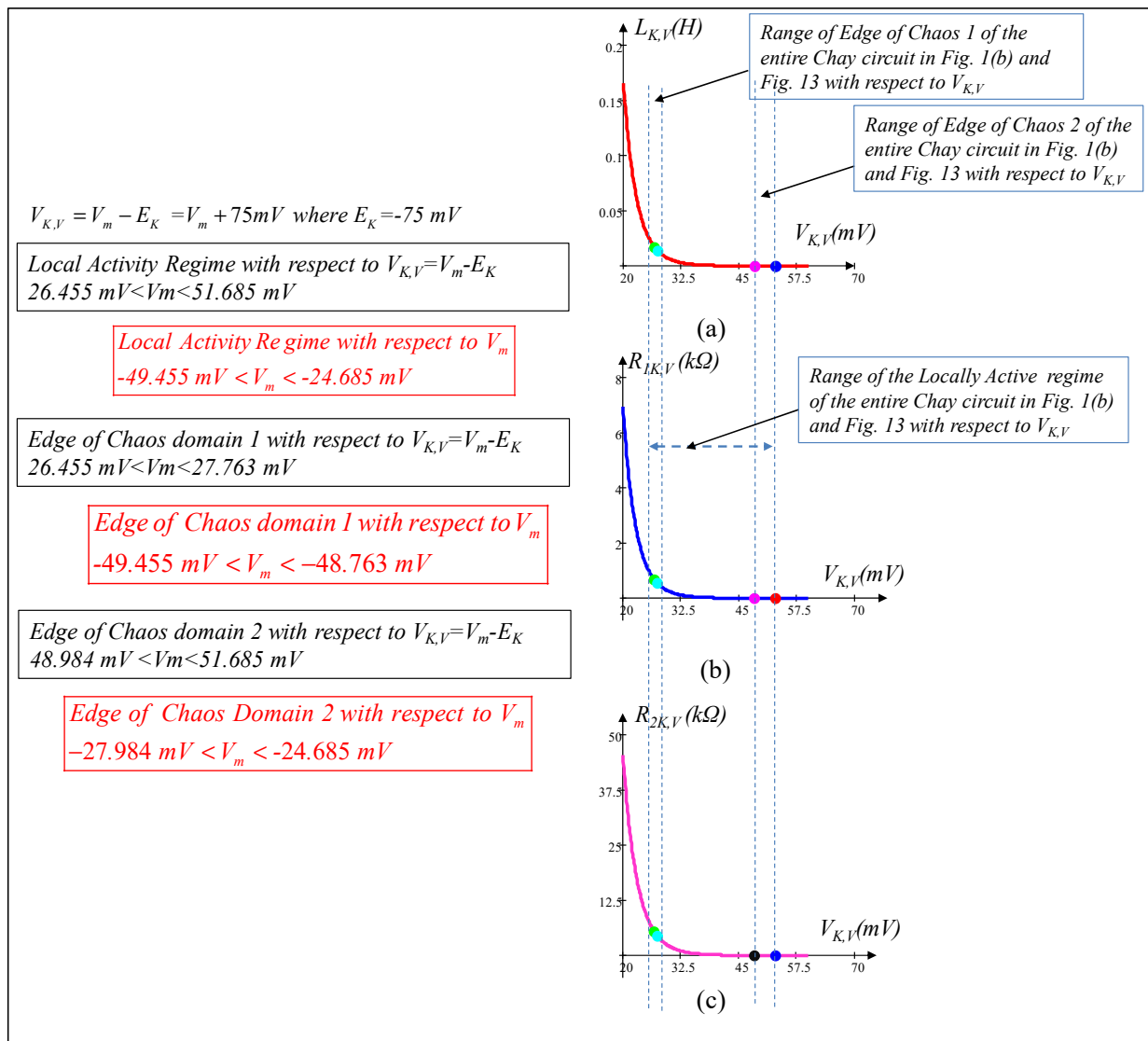


Figure 10. (a) Inductance $L_{K,V}$ (b) resistance $R_{1K,V}$ and (c) resistance $R_{2K,V}$ of the voltage-sensitive potassium ion channel memristor as a function of DC equilibrium voltage $V_{K,V} = V_m - E_K$ where $E_K = -75 mV$. $L_{K,V} > 0$, $R_{1K,V} > 0$ and $R_{2K,V} > 0$ shown in figures over the local activity, edge of chaos 1 and edge of chaos 2 are just corresponding range of the voltage with respect to $V_{K,V}$ of the entire connected Chay small signal equivalent circuit of Figure 1b and Figure 16.

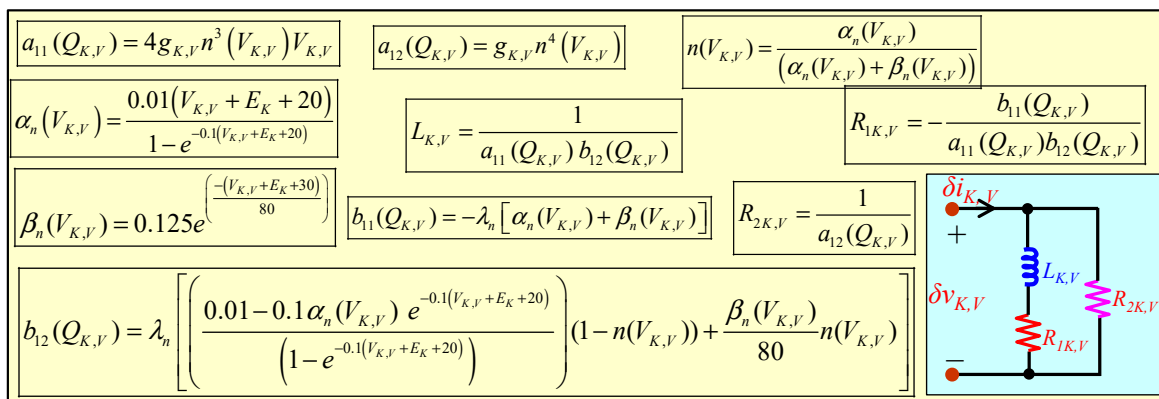


Figure 11. Explicit formulas for computing the coefficients $a_{11}(Q_{K,V})$, $a_{12}(Q_{K,V})$, $b_{11}(Q_{K,V})$, $b_{12}(Q_{K,V})$ and $L_{K,V}$, $R_{1K,V}$, $R_{2K,V}$ of the voltage-sensitive potassium ion channel memristor.

5.3. Small-Signal Circuit Model of the Calcium-Sensitive Potassium Ion Channel Memristor

The small-signal circuit model of the calcium-sensitive potassium-channel memristor at an equilibrium point $Q_{K,Ca}$ (The equilibrium point $Q_{K,Ca}$ at $v_{K,Ca} = V_{K,Ca}$ is obtained from Equation (23) by solving $f(Ca; V_{K,Ca}) = 0$ for $Ca = Ca_{Q_{K,Ca}}$. The explicit formula for $Ca(V_{K,Ca})$ is given in Figure 15.) in the DC $V_{K,Ca}$ - $I_{K,Ca}$ curve is derived by defining

$$Ca = Ca_{Q_{K,Ca}} + \delta Ca \tag{58}$$

$$v_{K,Ca} = V_{K,Ca}(Q_{K,Ca}) + \delta v_{K,Ca} \tag{59}$$

$$i_{K,Ca} = I_{K,Ca}(Q_{K,Ca}) + \delta i_{K,Ca} \tag{60}$$

Expanding $i_{K,Ca} = G_{K,Ca}(Ca) v_{K,Ca}$ from Equation (20) in a Taylor series about the equilibrium point $(Ca(Q_{K,Ca}), V_{Ca}(Q_{K,Ca}))$, we obtain

$$\begin{aligned} i_{K,Ca} &= a_{00}(Q_{K,Ca}) + a_{11}(Q_{K,Ca}) \delta Ca + a_{12}(Q_{K,Ca}) \delta v_{K,Ca} + h.o.t. \\ &= I_{K,Ca}(Q_{K,Ca}) + \delta i_{K,Ca} \end{aligned} \tag{61}$$

where

$$\delta Ca = Ca - Ca_{Q_{K,Ca}} \tag{62}$$

$$\delta v_{K,Ca} = v_{K,Ca} - V_{K,Ca}(Q_{K,Ca}) \tag{63}$$

$$\delta i_{K,Ca} = i_{K,Ca} - I_{K,Ca}(Q_{K,Ca}) \tag{64}$$

and

$$a_{00}(Q_{K,Ca}) = G_{Ca}(Q_{K,Ca}) V_{Ca}(Q_{K,Ca}) = I_{K,Ca}(Q_{K,Ca}) \tag{65}$$

$$a_{11}(Q_{K,Ca}) = V_{K,Ca}(Q_{K,Ca}) G'_{K,Ca}(Ca_{Q_{K,Ca}}) \tag{66}$$

$$a_{12}(Q_{K,Ca}) = G_{K,Ca}(Ca_{Q_{K,Ca}}) \tag{67}$$

and *h.o.t.* denotes the higher-order terms. Let us linearize the nonlinear equation by neglecting the *h.o.t.* in Equation (61), then:

$$\delta i_{K,Ca} = a_{11}(Q_{K,Ca}) \delta Ca + a_{12}(Q_{K,Ca}) \delta v_{K,Ca} \tag{68}$$

Similarly, expanding the state equation $f(Ca_{Q_{K,Ca}}, V_{K,Ca})$ of Equation (23) in a Taylor series about the equilibrium point $(Ca(Q_{K,Ca}), V_{Ca}(Q_{K,Ca}))$, we obtain

$$\begin{aligned} f(Ca_{Q_{K,Ca}} + \delta Ca, V_{K,Ca}(Q_{K,Ca}) + \delta v_{K,Ca}) \\ = f(Ca_{Q_{K,Ca}}, V_{Ca}(Q_{K,Ca})) + b_{11}(Q_{K,Ca}) \delta Ca + b_{12}(Q_{K,Ca}) \delta v_{K,Ca} + h.o.t. \end{aligned} \tag{69}$$

where

$$b_{11}(Q_{K,Ca}) = \left. \frac{\partial f(Ca, v_{K,Ca})}{\partial Ca} \right|_{Q_{K,Ca}} \tag{70}$$

$$b_{12}(Q_{K,Ca}) = \left. \frac{\partial f(Ca, v_{K,Ca})}{\partial v_{K,Ca}} \right|_{Q_{K,Ca}} \tag{71}$$

Linearizing the nonlinear state Equation (69) by neglecting the *h.o.t.*, we get

$$\frac{d(\delta Ca)}{dt} = b_{11}(Q_{K,Ca}) \delta Ca + b_{12}(Q_{K,Ca}) \delta v_{K,Ca} \tag{72}$$

Taking Laplace transform of Equations (68) and (72), we obtain

$$\hat{i}_{K,Ca}(s) = a_{11}(Q_{K,Ca}) \hat{C}a(s) + a_{12}(Q_{K,Ca}) \hat{v}_{K,Ca}(s) \tag{73}$$

$$s \hat{C}a(s) = b_{11}(Q_{K,Ca}) \hat{C}a(s) + b_{12}(Q_{K,Ca}) \hat{v}_{K,Ca}(s) \tag{74}$$

Solving Equation (74) for $C\hat{a}(s)$ and substituting the result into Equation (73), we obtain the following admittance $Y_{K,Ca}(s; Q_{K,Ca})$ of the small-signal equivalent circuit of the calcium-sensitive potassium ion channel memristor at equilibrium point $Q_{K,Ca}$:

$$Y_{K,Ca}(s; Q_{K,Ca}) = \frac{\hat{i}_{K,Ca}(s)}{\hat{v}_{K,Ca}(s)} = \left[\frac{1}{\frac{s}{a_{11}(Q_{K,Ca})b_{12}(Q_{K,Ca})} - \frac{b_{11}(Q_{K,Ca})}{a_{11}(Q_{K,Ca})b_{12}(Q_{K,Ca})}} + \frac{1}{\frac{1}{a_{12}(Q_{K,Ca})}} \right] \quad (75)$$

$$Y_{Ca}(s; Q_{Ca}) = \left(\frac{1}{(sL_{K,Ca} + R_{1K,Ca})} + \frac{1}{R_{2K,Ca}} \right) \quad (76)$$

$$\text{where } L_{K,Ca} \triangleq \frac{1}{a_{11}(Q_{K,Ca})b_{12}(Q_{K,Ca})} \quad (77)$$

$$R_{1K,Ca} \triangleq -\frac{b_{11}(Q_{K,Ca})}{a_{11}(Q_{K,Ca})b_{12}(Q_{K,Ca})} \quad (78)$$

$$R_{2K,Ca} \triangleq \frac{1}{a_{12}(Q_{K,Ca})} \quad (79)$$

It follows from Equations (77)–(79) that the small-signal admittance function of the first-order calcium-sensitive potassium ion channel memristor is equivalent to the series connection of an inductor and a resistor in parallel with another resistor, as shown in Figure 12. The corresponding coefficients a_{11} , a_{12} , b_{11} , b_{12} , and inductance $L_{K,Ca}$, resistance $R_{1K,Ca}$, and resistance $R_{2K,Ca}$ as a function of the DC equilibrium voltage $V_{K,Ca}$ are shown in Figures 13 and 14, respectively. The small-signal inductance and resistances (i.e., $L_{K,Ca} > 0$, $R_{1K,Ca} > 0$ and $R_{2K,Ca} > 0$) over the edge of chaos 1 and edge of chaos 2 with respect to the $V_{K,Ca}$ are shown in Figure 14a, Figure 14b, and Figure 14c, respectively. Please note that the local activity, edge of chaos 1 and edge of chaos 2, shown in Figure 14a–c, are not the local activity, edge of chaos 1 and edge of chaos 2 of the individual calcium-sensitive potassium ion channel memristor. The local activity and edge of chaos domains are just information showing the corresponding range of voltage with respect to $V_{K,Ca}$ when measured across the individual calcium-sensitive potassium ion channel memristor of the entire connected Chay small-signal equivalent circuit in Figure 1b and Figure 16. For the readers' convenience, the explicit formulas for computing the coefficients $a_{11}(Q_{K,Ca})$, $a_{12}(Q_{K,Ca})$, $b_{11}(Q_{K,Ca})$, $b_{12}(Q_{K,Ca})$ and $L_{K,Ca}$, $R_{1K,Ca}$, $R_{2K,Ca}$ are summarized in Figure 15.

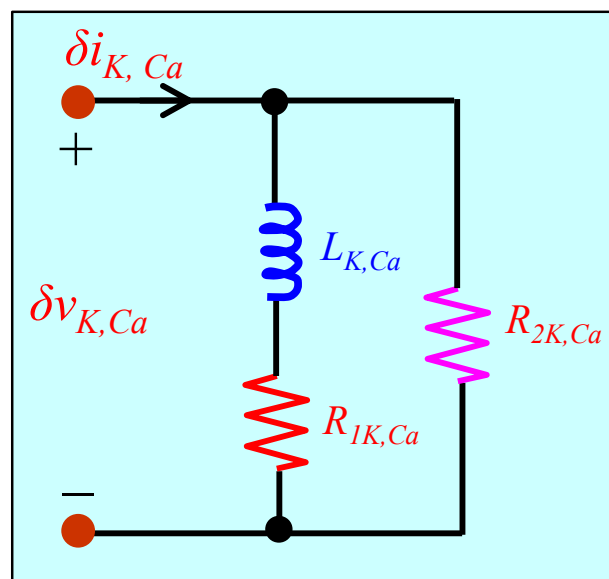


Figure 12. Small-signal equivalent circuit model of the calcium-sensitive potassium ion channel memristor about the DC equilibrium point $Q_{K,Ca}$ ($V_{K,Ca}$, $I_{K,Ca}$).

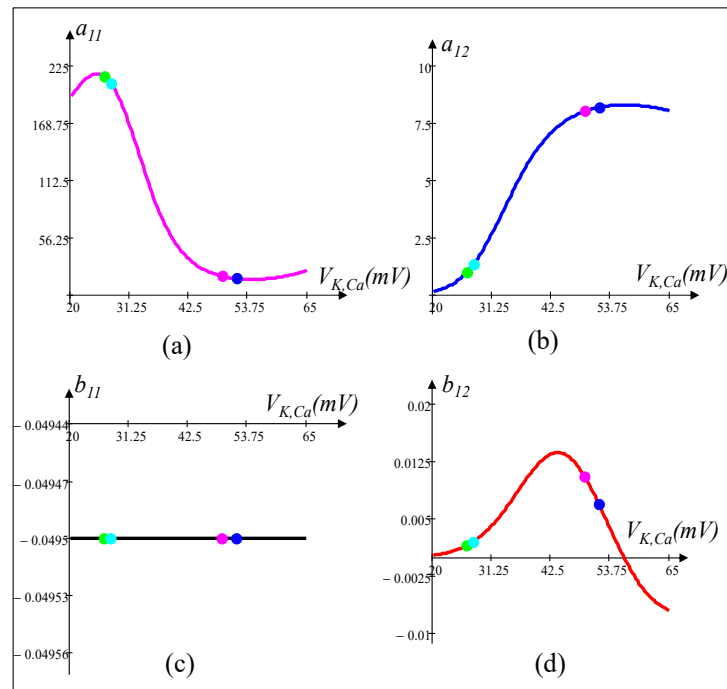


Figure 13. Plot of coefficients (a) a_{11} (b) a_{12} , (c) b_{11} , and (d) b_{12} of the calcium-sensitive potassium ion channel memristor as a function of the DC equilibrium voltage $V_{K,Ca}$.

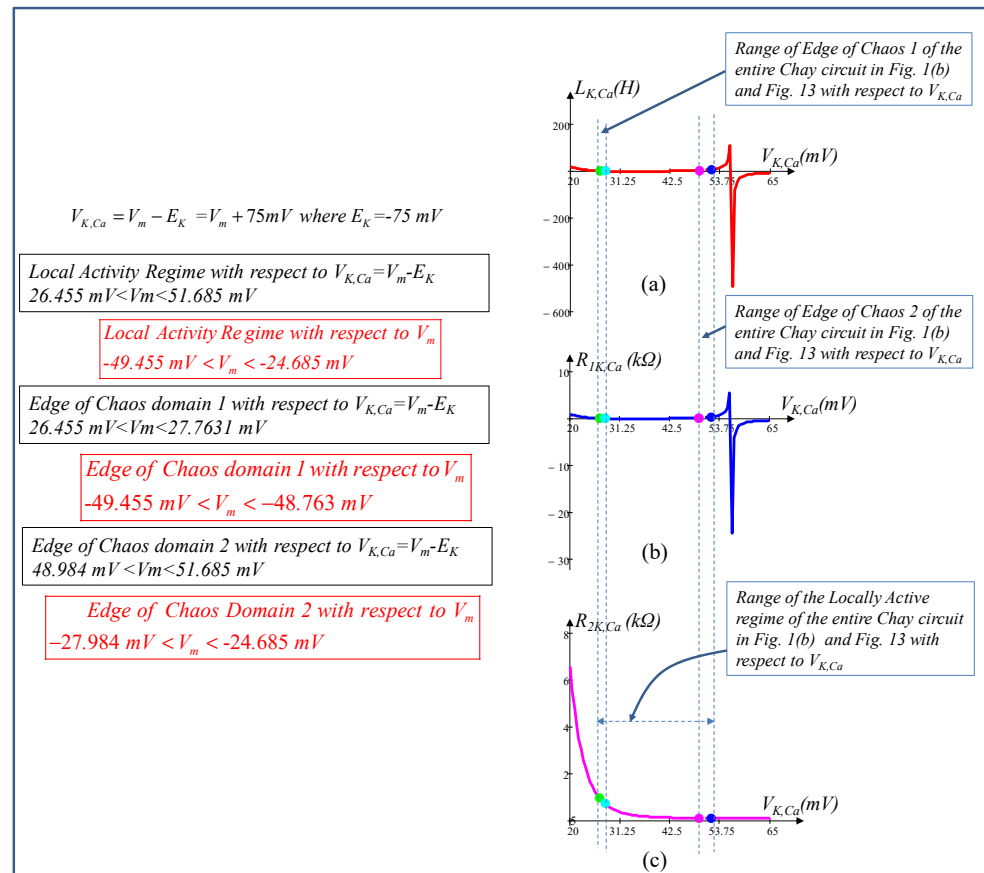


Figure 14. (a) Inductance $L_{K,Ca}$ (b) resistance $R_{1K,Ca}$ and (c) resistance $R_{2K,Ca}$ of the calcium-sensitive potassium ion channel memristor as a function of DC equilibrium voltage $V_{K,Ca}$. $L_{K,Ca} > 0$, $R_{1K,Ca} > 0$, and $R_{2K,Ca} > 0$ over the edge of chaos 1 and edge of chaos 2 with respect to $V_{K,Ca}$ of the entire connected Chay small-signal equivalent circuit of Figure 1b and Figure 16.

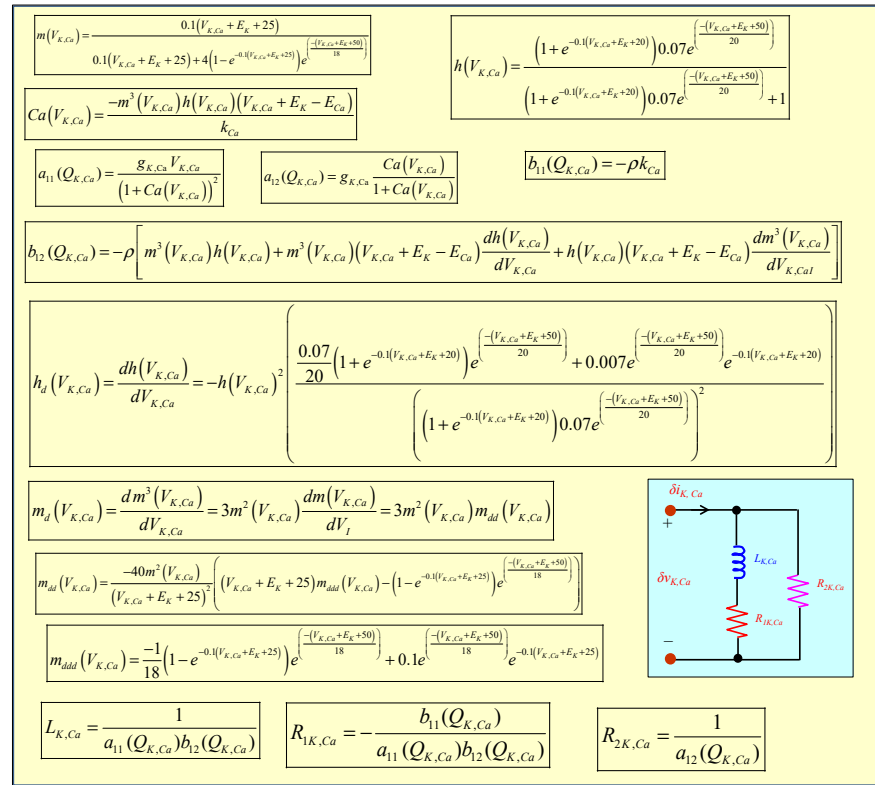


Figure 15. Explicit formulas for computing the coefficients $a_{11}(Q_{K,Ca})$, $a_{12}(Q_{K,Ca})$, $b_{11}(Q_{K,Ca})$, $b_{12}(Q_{K,Ca})$ and $L_{K,Ca}$, $R_{1K,Ca}$, $R_{2K,Ca}$ of the calcium-sensitive potassium ion channel memristor.

5.4. Small-Signal Circuit Model of the Memristive Chay Model

Let us replace the voltage-sensitive mixed ion channel nonlinear resistor, the voltage-sensitive potassium ion channel memristor, and the calcium-sensitive potassium ion channel memristor in the memristive Chay neuron circuit of Figure 1b with their small-signal models about DC operating voltages $V_I = V_m - E_I$, $V_{K,V} = V_m - E_K$, and $V_{K,Ca} = V_m - E_K$, respectively. Short-circuiting all the batteries, the equivalent small-signal circuit model of the third-order neuron circuit from Figure 1b about the operating point $V_m(Q)$ is found to be composed of one capacitor, two inductors, and six resistors, as shown in Figure 16. The local admittance $Y(s; V_m(Q))$ of this linear circuit seen from the port and formed by the capacitor terminals about Q is given by

$$Y(s; V_m(Q)) = sC_m + \frac{1}{sL_{K,V} + R_{1K,V}} + \frac{1}{sL_{K,Ca} + R_{1K,Ca}} + \frac{1}{R_{1,I}} + \frac{1}{R_{2K,V}} + \frac{1}{R_{2K,Ca}} + G_L \quad (80)$$

The corresponding ranges of local activity, edge of chaos 1 and edge of chaos 2, at equilibrium voltage $V_m(Q)$ (resp. I), are also given in Figure 16 for readers' convenience. We will cover the details of these regimes in the section on locally activity and edge of chaos. The circuit element $R_{1,I}$ is obtained by calculating the small signal model of the voltage-sensitive mixed ion channel nonlinear resistor from Figure 7 at equilibrium voltage $V_m(Q) = V_I + E_I$. Similarly, $L_{K,V}$, $R_{1K,V}$, and $R_{2K,V}$ are calculated from the small-signal equivalent circuit of the voltage-sensitive potassium ion channel memristor from Figure 11, and $L_{K,Ca}$, $R_{1K,Ca}$, and $R_{2K,Ca}$ are calculated from the small-signal equivalent circuit of the calcium-sensitive potassium ion channel memristor from Figure 15 at equilibrium voltage $V_m(Q)$, respectively. Note that $V_{K,V} + E_K$, and $V_{K,Ca} + E_K$ must be replaced by $V_m(Q)$ in Figures 11 and 15 by the small signal model of the voltage-sensitive potassium ion channel memristor and calcium-sensitive potassium ion channel memristor, respectively.

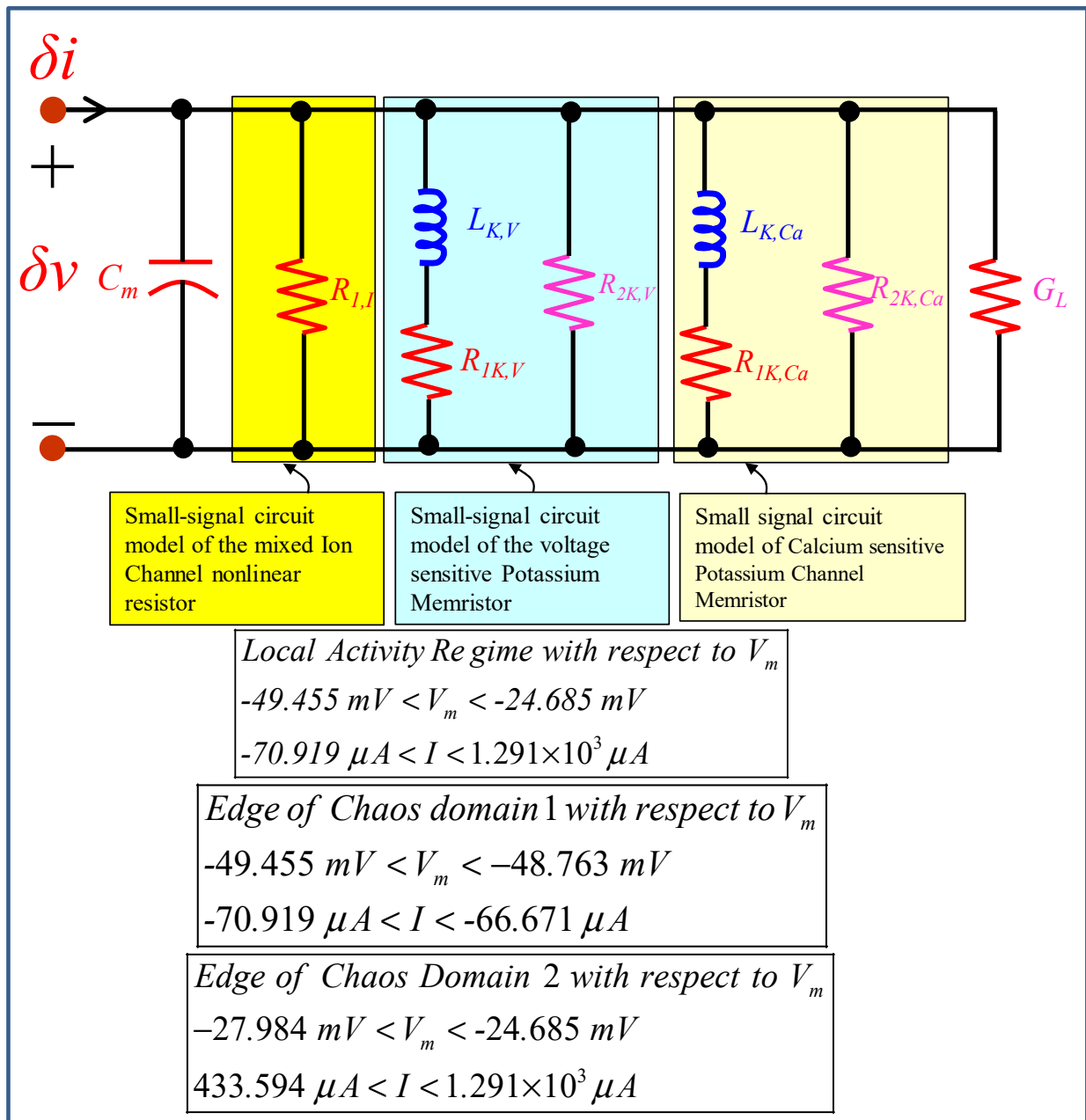


Figure 16. Small-signal equivalent circuit model of the memristive Chay model. The DC equilibrium voltage V_m is computed at $V_m = V_I + E_I$ for mixed ion channel non-linear resistor, $V_m = V_{K,V} + E_K$ for voltage-sensitive potassium ion channel memristor, and $V_m = V_{K,Ca} + E_K$ for calcium-sensitive potassium ion channel memristor, respectively.

5.4.1. Frequency Response

A convenient way to find the total admittance $Y(s; V_m(Q))$ by recasting Equation (80) into a rational function of the complex frequency variable s is as follows:

$$Y(s; V_m(Q)) = \frac{b_3 s^3 + b_2 s^2 + b_1 s + b_0}{a_2 s^2 + a_1 s + a_0} \quad (81)$$

where the explicit formulas for computing the coefficients $b_3, b_2, b_1, b_0, a_2, a_1,$ and a_0 are summarized in Figure 17.

$$\begin{aligned}
 b_3 &= L_{K,V} L_{K,Ca} R_{1,I} R_{2K,V} R_{2K,Ca} C_m \\
 b_2 &= (L_{K,V} R_{1K,ca} + L_{K,Ca} R_{1K,V}) R_{1,I} R_{2K,V} R_{2K,Ca} C_m + L_{K,V} L_{K,Ca} R_{2K,V} R_{2K,Ca} \\
 &\quad + L_{K,V} L_{K,Ca} R_{1,I} R_{2K,Ca} + L_{K,V} L_{K,Ca} R_{1,I} R_{2K,V} + L_{K,V} L_{K,Ca} R_{1,I} R_{2K,V} R_{2K,Ca} G_L \\
 b_1 &= R_{1,I} R_{1K,V} R_{1K,ca} R_{2K,V} R_{2K,Ca} C_m + (L_{K,Ca} R_{1,I} R_{2K,V} R_{2K,Ca}) + (L_{K,V} R_{1,I} R_{2K,V} R_{2K,Ca}) \\
 &\quad + (L_{K,V} R_{1K,ca} + L_{K,Ca} R_{1K,V}) R_{2K,V} R_{2K,Ca} + (L_{K,V} R_{1K,ca} + L_{K,Ca} R_{1K,V}) R_{1,I} R_{2K,Ca} \\
 &\quad + (L_{K,V} R_{1K,ca} + L_{K,Ca} R_{1K,V}) R_{1,I} R_{2K,V} + (L_{K,V} R_{1K,ca} + L_{K,Ca} R_{1K,V}) R_{1,I} R_{2K,V} R_{2K,Ca} G_L \\
 b_0 &= R_{1,I} R_{1K,ca} R_{2K,V} R_{2K,Ca} + R_{1,I} R_{1K,V} R_{2K,V} R_{2K,Ca} + R_{1K,V} R_{1K,ca} R_{2K,V} R_{2K,Ca} \\
 &\quad + R_{1,I} R_{1K,V} R_{1K,ca} R_{2K,Ca} + R_{1,I} R_{1K,V} R_{1K,ca} R_{2K,V} + R_{1,I} R_{1K,V} R_{1K,ca} R_{2K,V} R_{2K,Ca} G_L
 \end{aligned}$$

$$\begin{aligned}
 a_2 &= L_{K,V} L_{K,Ca} R_{1,I} R_{2K,V} R_{2K,Ca} \\
 a_1 &= (L_{K,V} R_{1K,ca} + L_{K,Ca} R_{1K,V}) R_{1,I} R_{2K,V} R_{2K,Ca} \\
 a_0 &= R_{1,I} R_{1K,V} R_{1K,ca} R_{2K,V} R_{2K,Ca}
 \end{aligned}$$

$$Y(s; V_m(Q)) = \frac{b_3 s^3 + b_2 s^2 + b_1 s + b_0}{a_2 s^2 + a_1 s + a_0}$$

Figure 17. Explicit formulas for computing the coefficients of $Y(s; V_m(Q))$.

Substituting $s = i\omega$ in Equation (81), we obtain the following small-signal admittance function at the equilibrium voltage $V_m(Q)$:

$$Y(i\omega; V_m(Q)) = \frac{(b_0 - b_2\omega^2)(a_0 - a_2\omega^2) + a_1\omega^2(b_1 - b_3\omega^2)}{(a_0 - a_2\omega^2)^2 + (a_1\omega)^2} + i\omega \left[\frac{[(b_1 - b_3\omega^2)(a_0 - a_2\omega^2) - a_1(b_0 - b_2\omega^2)]}{(a_0 - a_2\omega^2)^2 + (a_1\omega)^2} \right] \quad (82)$$

The corresponding real part $ReY(i\omega; V_m(Q))$ and imaginary part $ImY(i\omega; V_m(Q))$ from Equation (82) are given by,

$$\begin{aligned}
 ReY(i\omega; V_m(Q)) &= \left[\frac{(b_0 - b_2\omega^2)(a_0 - a_2\omega^2) + a_1\omega^2(b_1 - b_3\omega^2)}{(a_0 - a_2\omega^2)^2 + (a_1\omega)^2} \right] \\
 ImY(i\omega; V_m(Q)) &= \omega \left[\frac{[(b_1 - b_3\omega^2)(a_0 - a_2\omega^2) - a_1(b_0 - b_2\omega^2)]}{(a_0 - a_2\omega^2)^2 + (a_1\omega)^2} \right]
 \end{aligned} \quad (83)$$

Figure 18a,b show $ReY(i\omega; V_m(Q))$ vs. ω , $ImY(i\omega; V_m(Q))$ vs. ω , and the Nyquist plot $ImY(i\omega; V_m(Q))$ vs. $ReY(i\omega; V_m(Q))$ at the DC equilibrium voltage $V_m = -48.763$ mV (resp., $I = -66.671$ μ A), and $V_m = -27.984$ mV (resp., $I = 433.594$ μ A), respectively. Observe from Figure 18a,b that $ReY(i\omega; V_m(Q)) < 0$, thereby confirming the memristive Chay model is locally active at each of the two operating points. Our extensive numerical computations show the two DC equilibria coincide with two Hopf bifurcation points, which are the origin of the oscillation, spikes, chaos, and bursting in excitable cells. We will discuss these two bifurcation points in the next section with a pole-zeros and eigen values diagram.

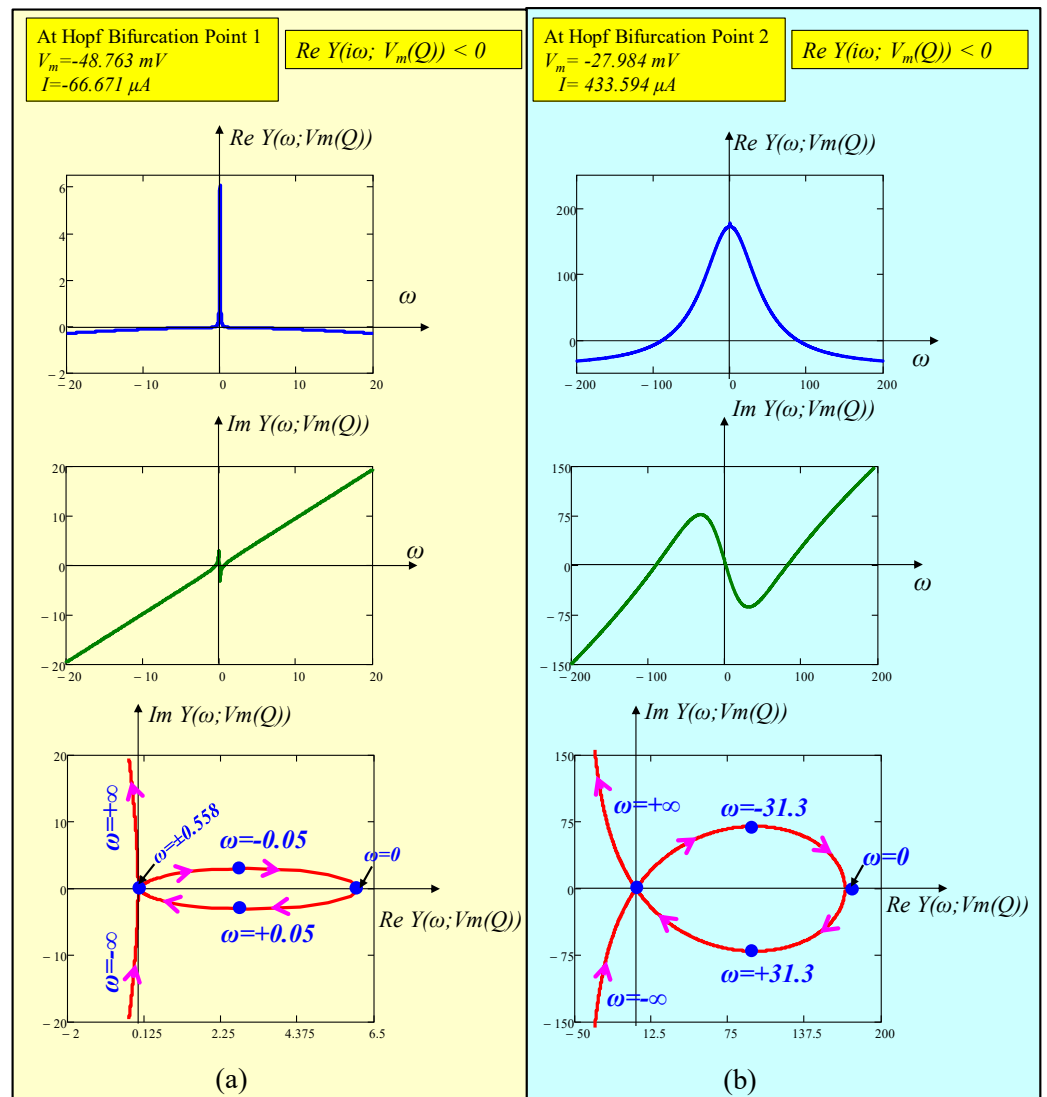


Figure 18. Small-signal admittance frequency response and Nyquist plot of the memristive Chay neuron model at (a) $V_m = -48.763$ mV (resp., $I = -66.671$ μ A) and (b) $V_m = -27.984$ mV (resp., $I = 433.594$ μ A). Observe that $ReY(i\omega; V_m(Q)) < 0$ at the two Hopf-bifurcation points.

5.4.2. Pole-Zero Diagram of the Small-Signal Admittance Function $Y(s; V_m(Q))$ and Eigen values of the Jacobian Matrix

The location of the poles and zeros of the small signal admittance function $Y(s; V_m(Q))$ of Equation (81) is computed by factorizing its denominator and numerators as

$$Y(s; V_m(Q)) = \frac{k(s - z_1)(s - z_2)(s - z_3)}{(s - p_1)(s - p_2)} \quad (84)$$

The poles of the small-signal admittance function $Y(s; V_m(Q))$ as a function of the voltage V_m over -200 mV $< V_m < 200$ mV is shown in Figure 19. Observe from Figure 19a,b that the two poles $Re(p_1), Re(p_2)$ are negative while $Im(p_1), Im(p_2)$ remain consistently zero for the specified DC input V_m . This observation confirms that the two poles of the admittance function possess no complex frequencies.

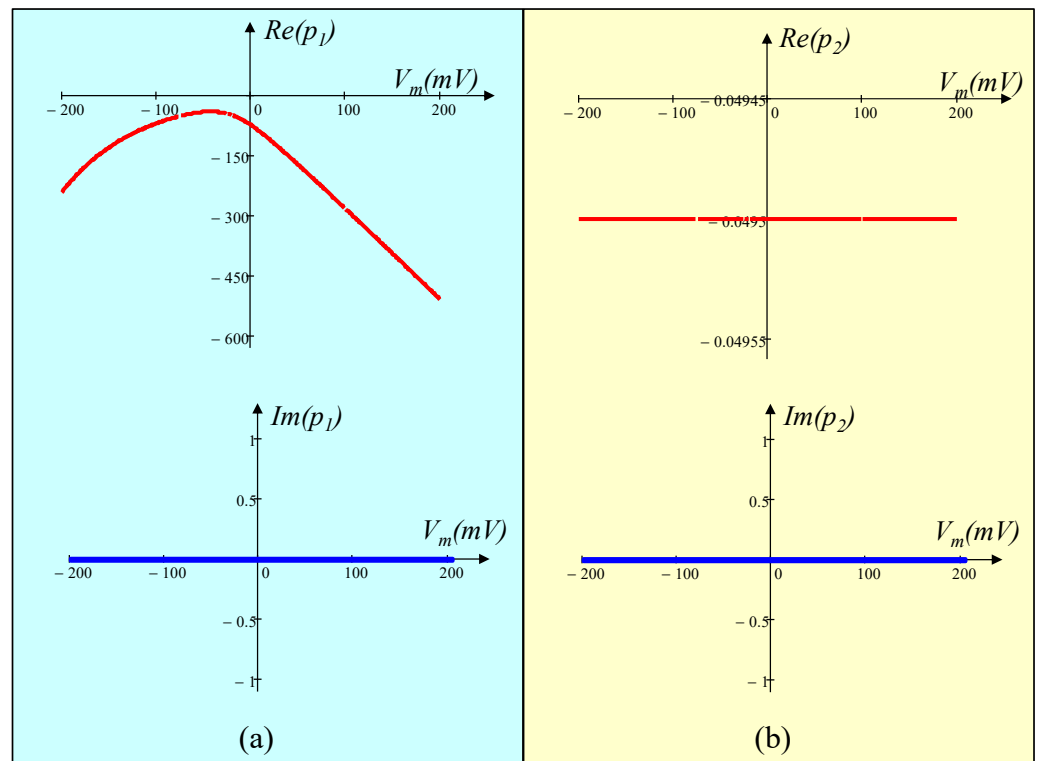


Figure 19. Poles diagram of the small-signal admittance function $Y(s; V_m(Q))$ as a function of V_m over $-200 \text{ mV} < V_m < 200 \text{ mV}$ (a) The top and bottom figures are the plots of the real part of pole 1 $Re(p_1)$ and the imaginary part of pole 1 $Im(p_1)$, respectively. (b) The top and bottom figures are the plots of the real part of pole 2 $Re(p_2)$ and the imaginary part of pole 2 $Im(p_2)$, respectively.

Figure 20a shows the *Nyquist plot*, i.e., loci of the imaginary part $Im(z_i)$ vs. the real part $Re(z_i)$ of the zeros as a function of the input voltage V_m over the interval $-55 \text{ mV} \leq V_m \leq 25 \text{ mV}$. Observe that the real parts of the two zeros z_2 and z_3 are zero at $V_m = -48.763 \text{ mV}$ (resp., $I = -66.671 \mu\text{A}$) and $V_m = -27.984 \text{ mV}$ (resp., $I = 433.594 \mu\text{A}$), respectively. The corresponding points when $Re(z_i) = 0$ are known as Hopf bifurcation points in bifurcation theory. Figure 20b,c show the zoomed version of Figure 20a near the two bifurcation points, respectively. It is also observed that the $Re(z_2)$ and $Re(z_3)$ lie in the open right half plane (RHP) between the bifurcation points $-48.763 \text{ mV} < V_m < -27.984 \text{ mV}$ (resp. $-66.671 \mu\text{A} < I < 433.594 \mu\text{A}$). Observe from Figure 21 that the eigen values, computed from the Jacobian matrix, associated with the ODEs (1)–(3) are identical to the zeros of the neuron local admittance $Y(s; V_m(Q))$, as inferable from Figure 20, and expected from the Chua theory [3,4].

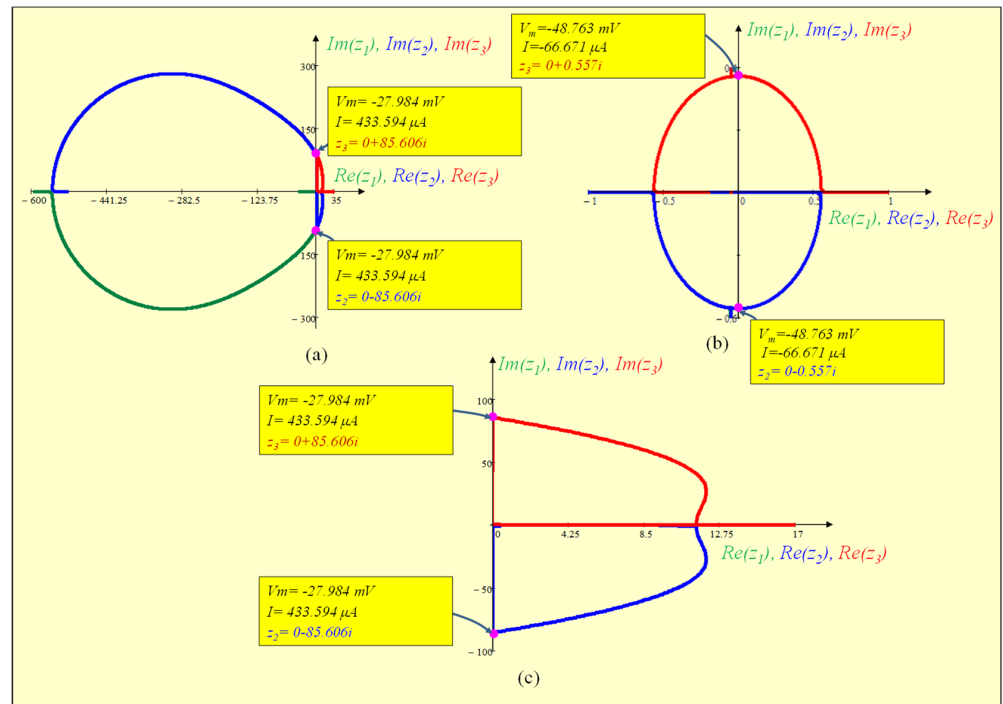


Figure 20. Zeros diagram of the small-signal admittance function $Y(s; V_m(Q))$ (a) Nyquist plot of the zeros z_1, z_2, z_3 in $Im(z_i)$ vs. $Re(z_i)$ plane (b) Nyquist plot near the Hopf-bifurcation point 1, $V_m = -48.763 \text{ mV}$ (resp., $I = -66.671 \mu\text{A}$). (c) Nyquist plot near the Hopf-bifurcation point 2, $V_m = -27.984 \text{ mV}$ (resp., $I = 433.594 \mu\text{A}$).

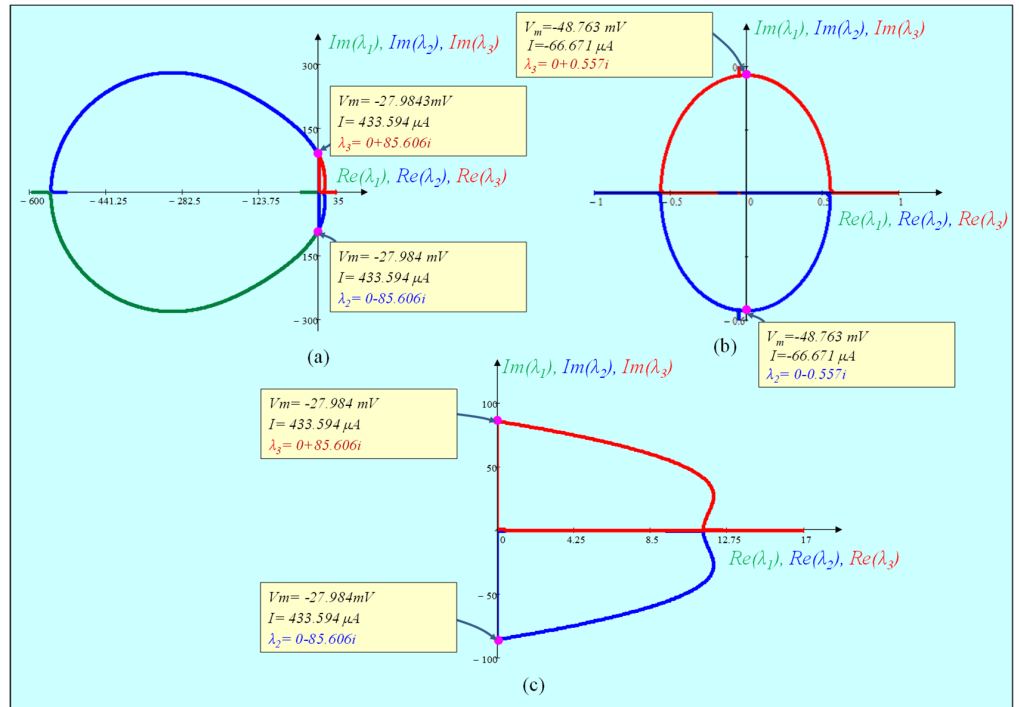


Figure 21. Plot of the loci of the eigen values of the Jacobian Matrix (a) Nyquist plot of the eigen values $\lambda_1, \lambda_2, \lambda_3$ in $Im(\lambda_i)$ vs. $Re(\lambda_i)$ plane. (b) Nyquist plot near the Hopf-bifurcation point 1, $V_m = -48.763 \text{ mV}$ (resp., $I = -66.671 \mu\text{A}$). (c) Nyquist plot near the Hopf-bifurcation point 2, $V_m = -27.984 \text{ mV}$ (resp., $I = 433.594 \mu\text{A}$). Our numerical computations confirm the zeros of the admittance functions $Y(s; V_m(Q))$ obtained in Figure 20 are identical to the eigen values of the Jacobian matrix.

6. Local Activity, Edge of Chaos, and Hopf-Bifurcation in Memristive Chay Model

Local activity and the edge of chaos are powerful mathematical and quantitative theories to predict whether a nonlinear system exhibits complexity or not. Local activity refers to a characteristic of nonlinear systems wherein infinitesimal fluctuations in energy are amplified, leading to the emergence of complex dynamical behavior in the system [34–44]. This section presents an extensive analysis of the memristive Chay model using the principles of local activity, the edge of chaos, and the Hopf-bifurcation theorem to predict the mechanism of generating the complicated electrical signals in an excitable cell.

6.1. Locally Active Regime

The local activity theorem developed by Chua reveals that a nonlinear system must satisfy at least one of the following conditions, concerning its local transfer function about a given operating point in order to support the emergence of complexity [36].

(i) The zero of the admittance function $Y(s; V_m(Q))$ lie in the open-right plane where $Re(s_z) > 0$.

(ii) $Y(s; V_m(Q))$ has multiple zeros on the imaginary axis.

(iii) $Y(s; V_m(Q))$ has a simple zero on the imaginary axis $s = i\omega_z$ on the imaginary axis and $K_Q(i\omega_z) \triangleq \lim_{s \rightarrow i\omega_z} (s - i\omega_z)Y(s; V_m(Q))$ is either a negative real number or a complex number.

(iv) $ReY(i\omega; V_m(Q)) < 0$ for some $\omega \in [-\infty, +\infty]$.

In other words, the emergence of action potentials, chaos, bursting, or spikes in neurons are impossible unless the cells are locally active. Therefore, restricting the behavior of a nonlinear system to its local activity operating regime reduces the considerable time necessary to identify the complex phenomena that may emerge across its physical medium as compared with a standard trial-and-error numerical investigation. In order to restrict the above dynamical behavior in the memristive Chay model of an excitable cell in the local activity regime, we performed comprehensive numerical analyses within the range of the DC equilibrium voltage $V_m = -50$ mV (resp. $I = -74.316$ μ A) to $V_m = -23.5$ mV (resp. $I = 1.76 \times 10^3$ μ A). Observe from Figure 22a the real part of the admittance of the frequency response $ReY(i\omega; V_m(Q)) > 0$ at $V_m = -50$ mV (resp. $I = -74.316$ μ A), thereby confirming locally passive at this equilibrium point. However, when $V_m > -50$ mV, our in-depth simulation in Figure 22b shows that $ReY(i\omega; V_m(Q)) = 0$ at $V_m = -49.455$ mV (resp. $I = -70.919$ μ A) and Figure 22c,d show that $ReY(i\omega; V_m(Q)) < 0$ at $V_m = -48.1$ mV (resp. $I = -62.681$ μ A) and $V_m = -26.5$ mV (resp. $I = 746.457$ μ A) respectively for some frequency ω , confirming an excitable cell is locally active at these equilibria. Our simulations in Figure 22e shows a further increase in the DC equilibrium voltage at $V_m = -24.685$ mV (resp. $I = 1.291 \times 10^3$ μ A), and the loci are tangential to the ω axis, i.e., $ReY(i\omega; V_m(Q)) = 0$. However, when $V_m > -24.685$ mV, say $V_m = -23.5$ mV (resp. $I = 1.76 \times 10^3$ μ A), it is observed from Figure 22f that $Re Y(i\omega; V_m(Q)) > 0$, and the memristive Chay model is no more locally active, confirming the cell is locally passive at this equilibrium. Therefore, the local activity regime that started above $V_m = -49.455$ mV (resp. $I = -70.919$ μ A) exists over the following regime

$$\begin{aligned} & \text{Local Activity Regime} \\ & -49.455 \text{ mV} < V_m < -24.685 \text{ mV} \\ & -70.919 \text{ } \mu\text{A} < I < 1.291 \times 10^3 \text{ } \mu\text{A} \end{aligned} \tag{85}$$

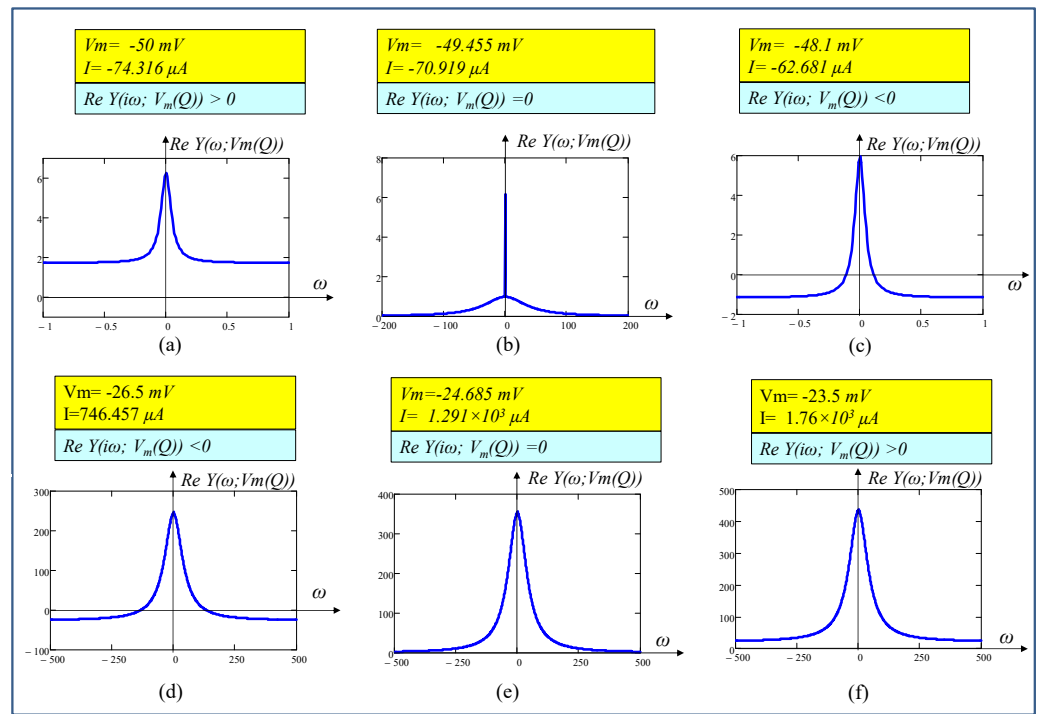


Figure 22. Plot of $Re(i\omega; V_m(Q))$ to illustrate the local activity principle at (a) $V_m = -50$ mV (resp. $I = -74.316$ μ A) (b) $V_m = -49.455$ mV (resp. $I = -70.919$ μ A), (c) $V_m = -48.1$ mV (resp. $I = -62.681$ μ A), (d) $V_m = -26.5$ mV (resp. $I = 746.457$ μ A), (e) $V_m = -24.685$ mV (resp. $I = 1.291 \times 10^3$ μ A), (f) $V_m = -23.5$ mV (resp. $I = 1.76 \times 10^3$ μ A), respectively.

6.2. Edge of Chaos Regime

The edge of chaos is a tiny subset of the locally active domain where the zeros of the admittance function $Y(s; V_m(Q))$ (equivalent to the eigen values of the Jacobian matrix) lie in the open left-half plane, i.e., $Re(z_p) < 0$ (eigen values $\lambda_i < 0$) as well as $Re Y(i\omega; V_m(Q)) < 0$. Figure 21a,b show the real part of the eigen values vanish at $V_m = -48.7631$ mV (resp. $I = -66.671$ μ A) with a pair of complex eigen values $\lambda_{2,3} = \pm 0.557i$. It follows from the edge of chaos theorem that the corresponding equilibrium point is no longer asymptotically stable and becomes unstable thereafter, confirming the *first edge of chaos* regime over the following small interval:

$$\begin{aligned} & \text{Edge of chaos domain 1} \\ & -49.455 \text{ mV} < V_m < -48.763 \text{ mV} \\ & -70.919 \text{ } \mu\text{A} < I < -66.671 \text{ } \mu\text{A} \end{aligned} \tag{86}$$

Observe from Figure 21c that the real part of the eigen values vanish at $\lambda_{2,3} = \pm 85.606i$ at DC equilibrium voltage $V_m = -27.984$ mV (resp. $I = 433.594$ μ A). It follows that the corresponding equilibrium point $V_m(Q)$ is no longer asymptotically stable below this equilibrium point, therefore confirming the existence of a *second edge of chaos* regime over the following interval:

$$\begin{aligned} & \text{Edge of chaos Domain 2} \\ & -27.984 \text{ mV} < V_m < -24.685 \text{ mV} \\ & 433.594 \text{ } \mu\text{A} < I < 1.291 \times 10^3 \text{ } \mu\text{A} \end{aligned} \tag{87}$$

The nonlinear dynamical behavior of the memristive Chay model in this paper is controlled by the function of the input stimulus I. The local activity, edge of chaos 1 and edge of chaos 2 regimes are computed in this paper under the assumption of departing

the input parameter I from lower stimulus to higher stimulus (resp. low DC equilibrium voltage $V_m(Q)$ to high equilibrium voltage $V_m(Q)$).

6.3. Hopf-Bifurcation

Hopf-bifurcation namely, super-critical and sub-critical bifurcations are local bifurcation phenomena in which an equilibrium point changes its stability as the parameter of the nonlinear system changes under certain conditions. An unstable equilibrium point surrounded by a stable limit cycle results in a super-critical Hopf bifurcation, whereas a subcritical Hopf bifurcation refers to a qualitative change in the behavior of a system where a stable equilibrium point transitions to instability, giving rise to sustained oscillations or limit cycles as a parameter is varied. Our careful simulation at Hopf-bifurcation point 1 at $V_m = -48.763$ mV (resp. $I = -66.671$ μ A) (*The supercritical Hopf bifurcation points 1 and 2 observed in this paper are based on the numerical simulations and for the parameters listed in Table 2. The bifurcation phenomenon may vary for different parameters and environments.*) shows that stimulus current I should be chosen within the very small edge of chaos domain 1, where the real part of the eigen values are negative. The result converges to DC equilibrium for any initial conditions. Likewise, if I is selected within bifurcation point 1, where the real part of the eigen values are positive, the result converges to a stable limit cycle. Therefore, it follows from the bifurcation theory that bifurcation point 1 is a super-critical Hopf bifurcation. Figure 23a,b show the numerical simulations at $I = -68.118$ μ A and $I = -65.077$ μ A, respectively. Observe from Figure 23a,b that $I = -68.118$ μ A lying within the tiny subset of edge of chaos domain 1 converges to DC equilibrium and $I = -65.077$ μ A lying in the open right half-plane (RHP) converges to spikes, respectively, confirming that bifurcation point 1 is a super-critical Hopf bifurcation.

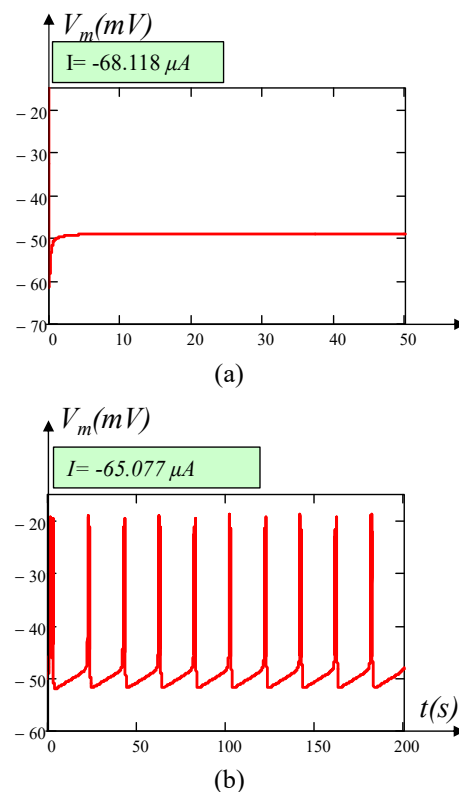


Figure 23. Numerical simulations to confirm the super-critical Hopf bifurcation at bifurcation point 1. Plot of membrane potential V_m at (a) $I = -68.118$ μ A which lies inside the tiny subset of edge of chaos domain 1 and beyond bifurcation point 1 converges to the DC equilibrium; (b) $I = -65.077$ μ A, chosen just to the right of bifurcation point 1, where the real parts of two zeros of the neuron local admittance lie on the open right half plane (RHP), converges to the spikes.

Similarly, our careful examination predicts a stable DC equilibrium point when current I is chosen within a very small edge of chaos 2, confirming supercritical Hopf bifurcation at bifurcation point $V_m = -27.984$ mV (resp. $I = 433.594$ μ A). The possibility of the above scenario is illustrated in Figure 24. Figure 24a shows the membrane potential V_m converges to a stable DC equilibrium point when $I = 440$ μ A, chosen within the edge of chaos domain 2. Figure 24b shows that when $I = 430.884$ μ A, chosen very close and inside the bifurcation point 2, where the real part of the eigenvalue is positive and lies in the open right half plane (RHP), the transient waveform converges to a stable limit cycle as predicted by the Hopf super critical bifurcation theorem.

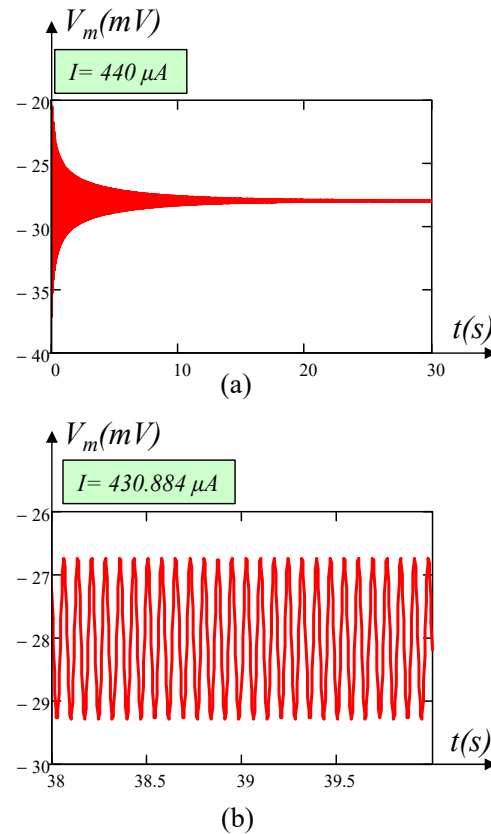


Figure 24. Numerical simulations to confirm the super-critical Hopf bifurcation at bifurcation point 2. (a) Plot of membrane potential V_m which converges to stable DC equilibrium when $I = 440$ μ A chosen inside the tiny subset of edge of chaos domain 2 and near and beyond the bifurcation point 2. (b) Membrane potential converging to oscillation as predicted by the Hopf bifurcation theorem when $I = 430.884$ μ A is chosen inside the bifurcation point (open right-half plane).

Table 3 illustrates the computation of the potassium ion channel activation n , calcium concentration Ca , and eigen values (λ_1 , λ_2 , and λ_3) as a function of the DC stimulus current I (resp. membrane potential V_m) at the DC equilibrium point Q . It is observed from Table 3 and Figure 21a,c that the two Hopf bifurcations points 1 and 2 occur at $V_m = -48.763$ mV (resp. $I = -66.671$ μ A) and $V_m = -27.984$ mV (resp. $I = 433.594$ μ A), respectively, where the eigen values are purely imaginary at these two equilibria. As I decreases (resp. V_m decreases) from Hopf bifurcation point 1, the eigen values migrate to the left-hand side, confirming the real parts of the eigen values are no longer positive and thereby confirming the first negative real eigen values regime exists over the following interval.

| | |
|--|------|
| Negative real eigen values regime 1 : $-\infty < V_m < -48.763 \text{ mV}$ $-\infty < I < -66.671 \text{ } \mu\text{A}$ | (88) |
|--|------|

Table 3. Computation of the potassium ion channel activation n , calcium concentration Ca , and eigen values (λ_1, λ_2 , and λ_3) as a function of the stimulus current I (resp. membrane potential V_m). Rows 5 to 7 pertain to the edge of chaos 1, rows 8 to 16 pertain to the unstable local activity domain, and rows 17 to 20 pertain to the edge of chaos 2. Rows 7 and 17 pertain to Hopf bifurcation points 1 and 2, respectively, for the memristive Chay neuron model.

| S.N | V_m (mV) | I (μA) | n | Ca | λ_1 | λ_2 | λ_3 |
|-----|------------|---------------------|------|------|--------------------|--------------------|------------------|
| 1. | -52.00 | -87.02 | 0.08 | 0.04 | -40.515 | -3.842 | -0.084 |
| 2. | -51.00 | -80.63 | 0.08 | 0.05 | -40.107 | -2.871 | -0.111 |
| 3. | -50.50 | -77.46 | 0.09 | 0.06 | -39.891 | -2.289 | -0.139 |
| 4. | -50.00 | -74.32 | 0.09 | 0.07 | 39.666 | -1.617 | -0.196 |
| 5. | -49.455 | -70.919 | 0.94 | 0.08 | -39.408 | -0.533 - 0.174i | -0.533 + 0.174i |
| 6. | -49.00 | -68.12 | 0.1 | 0.1 | -39.181 | -0.19 - 0.525i | -0.19 + 0.525i |
| 7. | -48.763 | -66.671 | 0.1 | 0.1 | -39.058 | 0 - 0.557i | 0 + 0.557i |
| 8. | -48.50 | -65.08 | 0.1 | 0.11 | -38.917 | 0.222 - 0.51i | 0.2215 + 0.5097i |
| 9. | -46.00 | -51.02 | 0.12 | 0.21 | -37.32 | 0.046 | 5.736 |
| 10. | -45.00 | -46.37 | 0.13 | 0.27 | -36.512 | 0.027 | 8.498 |
| 11. | -42.00 | -39.37 | 0.16 | 0.53 | -33.218 | 0.0001 | 18.604 |
| 12. | -40.00 | -42.78 | 0.18 | 0.79 | -29.899 | -0.0084 | 25.99 |
| 13. | -38.00 | -51.26 | 0.21 | 1.13 | -24.898 | -0.0112 | 31.992 |
| 14. | -32.00 | 17.59 | 0.29 | 2.57 | -0.061 | 11.669 - 38.01i | 11.669 + 38.01i |
| 15. | -30.00 | 160.68 | 0.32 | 3.12 | -0.053 | 8.049 - 61.778i | 8.049 + 61.778i |
| 16. | -28.00 | 430.84 | 0.35 | 3.65 | -0.051 | 0.08 - 85.421i | 0.08 + 85.421i |
| 17. | -27.984 | 433.594 | 0.35 | 3.65 | -0.051 | 0 - 85.606i | 0 + 85.606i |
| 18. | -27.00 | 628.91 | 0.36 | 3.89 | -5.556 - 97.197i | -5.556 + 97.197i | -0.051 |
| 19. | -25.50 | 1.02×10^3 | 0.39 | 4.22 | -15.942 - 114.607i | -15.942 + 114.607i | -0.0501 |
| 20. | -24.685 | 1.291×10^3 | 0.40 | 4.37 | -22.466 - 123.858i | -22.466 + 123.858i | -0.0499 |
| 21. | -23.00 | 1.99×10^3 | 0.43 | 4.64 | -37.643 - 142.384i | -37.643 + 142.384i | -0.0497 |
| 22. | -22.00 | 2.5×10^3 | 0.44 | 4.75 | -47.529 - 152.923i | -47.529 + 152.923i | -0.0496 |

Similarly, as I increases (resp. V_m increases) from the second bifurcation points, the positive real part of the eigen values migrates from the open right half to the open left half, confirming the second negative real eigen values regime over the following interval:

$$\begin{aligned}
 &\text{Negative real eigen values regime 2 :} \\
 &\quad -27.984 \text{ mV} < V_m < +\infty \\
 &\quad 433.594 \mu A < I < +\infty
 \end{aligned}
 \tag{89}$$

Observe from Table 3 and Figure 21a–c that two eigen values of the Jacobian matrix associated with the ODE set Equations (1)–(3) lie on the open RHP for each operating point Q corresponding to a DC current I value between Hopf bifurcation point 1 and Hopf bifurcation point 2. Therefore, the generation of periodic, bursting, spikes, and chaos signals predicted by the Hopf bifurcation theorem in an excitable cell exists over the following interval:

$$\begin{aligned}
 &\text{Unstable (periodic, bursting, chaos, spikes) regime :} \\
 &\quad -48.763 \text{ mV} < V_m < -27.984 \text{ mV} \\
 &\quad -66.671 \mu A < I < 433.594 \mu A
 \end{aligned}
 \tag{90}$$

The convergence of the membrane potential to stable and unstable DC equilibrium points is verified by numerical simulations at different values of I and is illustrated in Figure 25. Figure 25a shows the transient waveform of membrane potential V_m converging to a stable DC equilibrium at $I = -90 \mu\text{A}$, confirming the Hopf bifurcation theorem no longer holds at this equilibrium. Similarly, when DC stimulus currents $I = -50 \mu\text{A}$ and $-10 \mu\text{A}$ are chosen inside the two bifurcation points $I = -66.671 \mu\text{A}$ and $I = 433.594 \mu\text{A}$, we observed different patterns of oscillations as shown in Figure 25b,c, confirming the bifurcation theorem holds in this regime. Likewise, when DC stimulus currents $I = 10 \mu\text{A}$ and $I = 2000 \mu\text{A}$ are applied within the bifurcation points $I = -66.671 \mu\text{A}$ and $I = 433.594$, respectively, oscillation patterns emerge as depicted in Figure 26a,b. Similarly, Figure 26c illustrates the transient waveform of the membrane potential V_m , indicating its convergence to a stable DC equilibrium at $I = 500 \mu\text{A}$. This observation suggests that the Hopf bifurcation theorem no longer holds at this equilibrium point.

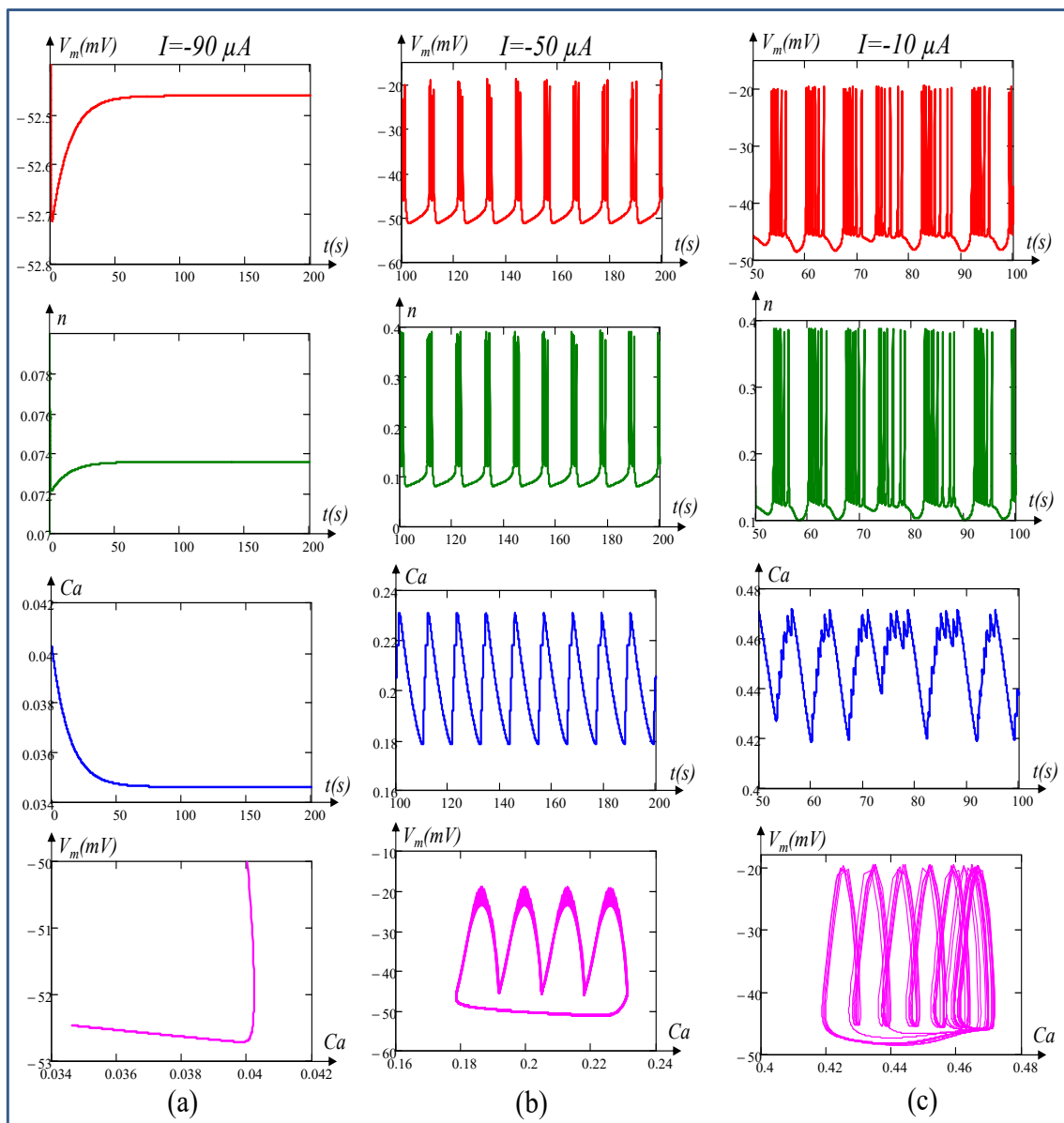


Figure 25. Patterns of oscillations when stimulus current I is chosen beyond and inside the bifurcation points. (a) DC pattern observed when $I = -90 \mu\text{A}$ chosen beyond bifurcation point 1 ($I = -66.671 \mu\text{A}$). Different patterns of oscillations occur when I is chosen between the two bifurcation points $I = -66.671 \mu\text{A}$ and $I = 433.594 \mu\text{A}$ at (b) $I = -50 \mu\text{A}$ and (c) $I = -10 \mu\text{A}$.

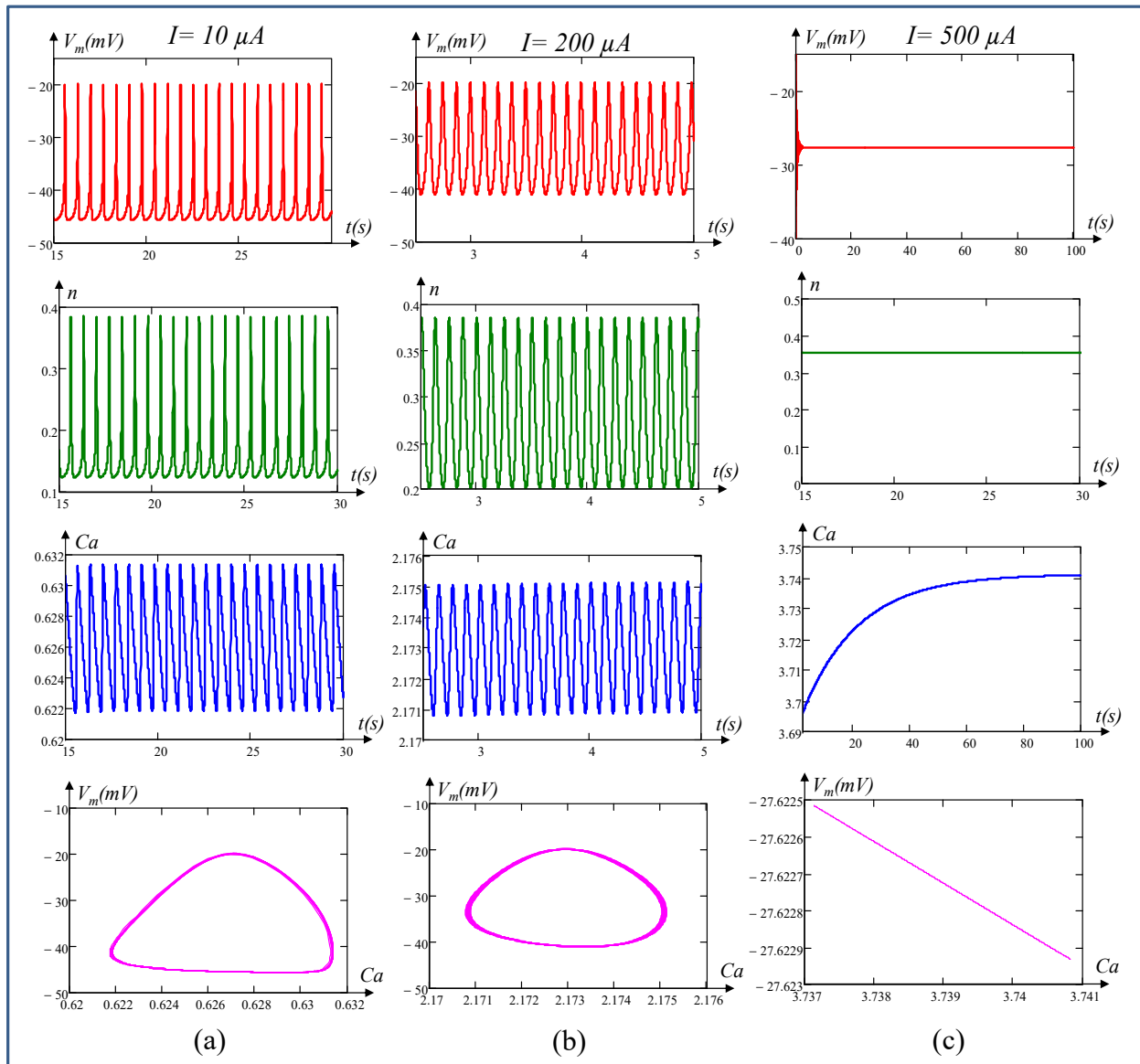


Figure 26. Patterns of oscillations when stimulus current I is chosen inside and beyond the bifurcation points. Oscillation patterns when I is chosen between the two bifurcation points $I = -66.671 \mu A$ and $I = 433.594 \mu A$, at (a) $I = 10 \mu A$, and (b) $I = 200 \mu A$. (c) The DC pattern when $I = 500 \mu A$ is chosen beyond bifurcation point 2 ($I = 433.594 \mu A$).

Figures 27 and 28 show the different patterns of oscillations when the conductance g_{KCa} of the calcium-sensitive potassium ion channel memristor is varied from 10 mS/cm^2 to 11.5 mS/cm^2 at stimulus current $I = 0$. Figure 27a shows the excitable membrane cell has a stable limit cycle with period one at $g_{K,Ca} = 10 \text{ mS/cm}^2$. As the parameter $g_{K,Ca}$ increases to 10.7 mS/cm^2 , 10.75 mS/cm^2 , and 10.77 mS/cm^2 , the cell fires periods two, four, and eight, as shown in Figure 27b, Figure 27c, and Figure 28a, respectively. The change in period doubling is more apparent in calcium concentration (Ca) vs. time and V_m vs. Ca , as shown at the bottom of Figure 27b, Figure 27c, and Figure 28a, respectively. Figure 28b shows the waveform of the memristive Chay model, confirming the existence of aperiodic oscillation (chaos) at $g_{K,Ca} = 11 \text{ mS/cm}^2$. The firing of aperiodic oscillations from the cell can be clearly seen from the plot of Ca vs. time and V_m vs. Ca in Figure 28b. A further increase in $g_{K,Ca}$ to 11.5 mS/cm^2 gives rise to the firing of the cell from aperiodic to rhythmic bursting, as shown in Figure 28c.

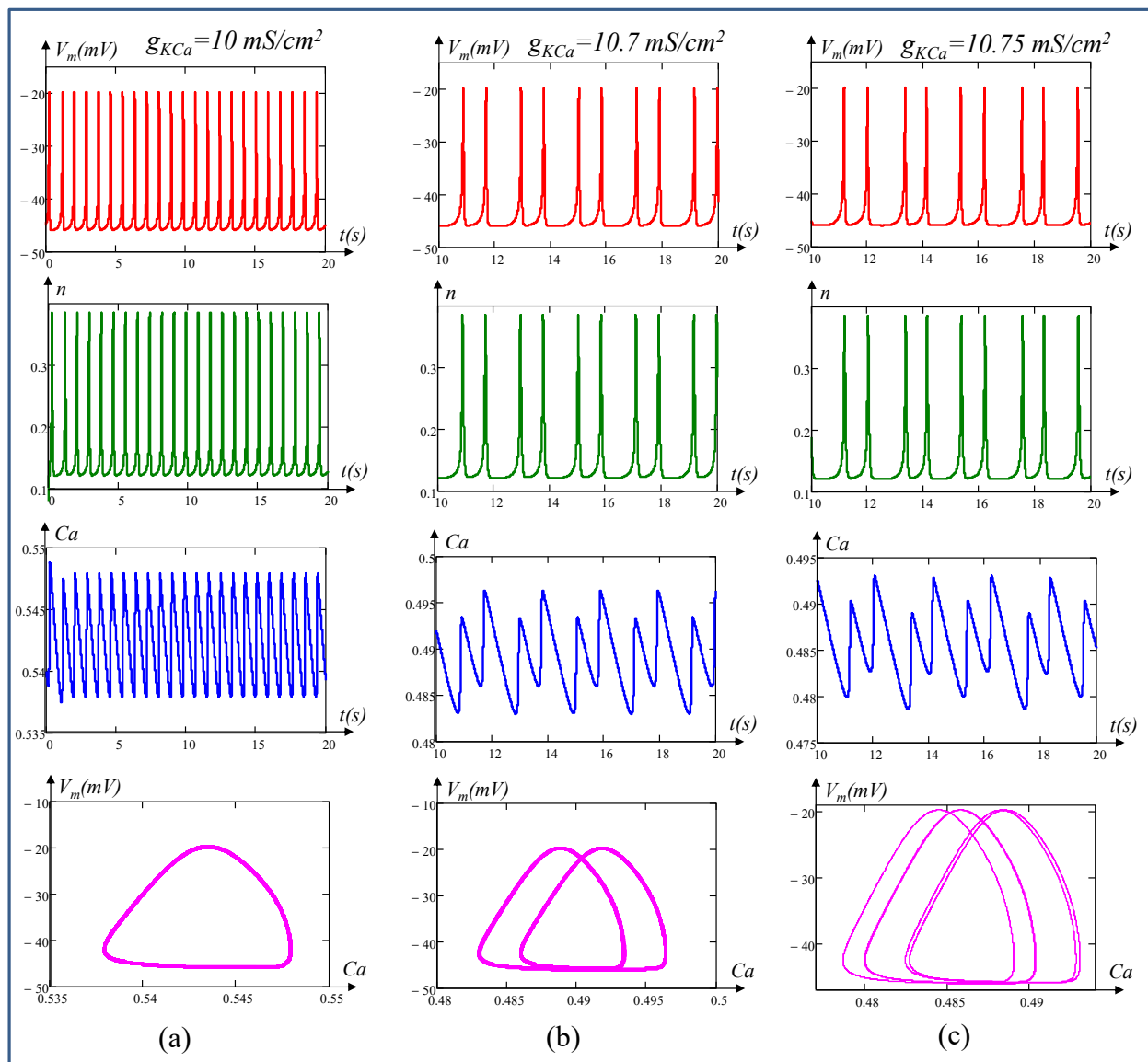


Figure 27. Different patterns of oscillations when g_{KCa} varied from 10 mS/cm^2 to 10.75 mS/cm^2 at DC stimulus current $I = 0$. (a) Period-1 oscillation at $g_{K,Ca} = 10 \text{ mS/cm}^2$ (b) Period-2 oscillation at $g_{K,Ca} = 10.7 \text{ mS/cm}^2$ (c) Period-4 oscillation at $g_{K,Ca} = 10.75 \text{ mS/cm}^2$. The simulations were performed at the initial conditions $V_m(0) = -50 \text{ mV}$, $n(0) = 0.1$, and $Ca(0) = 0.48$.

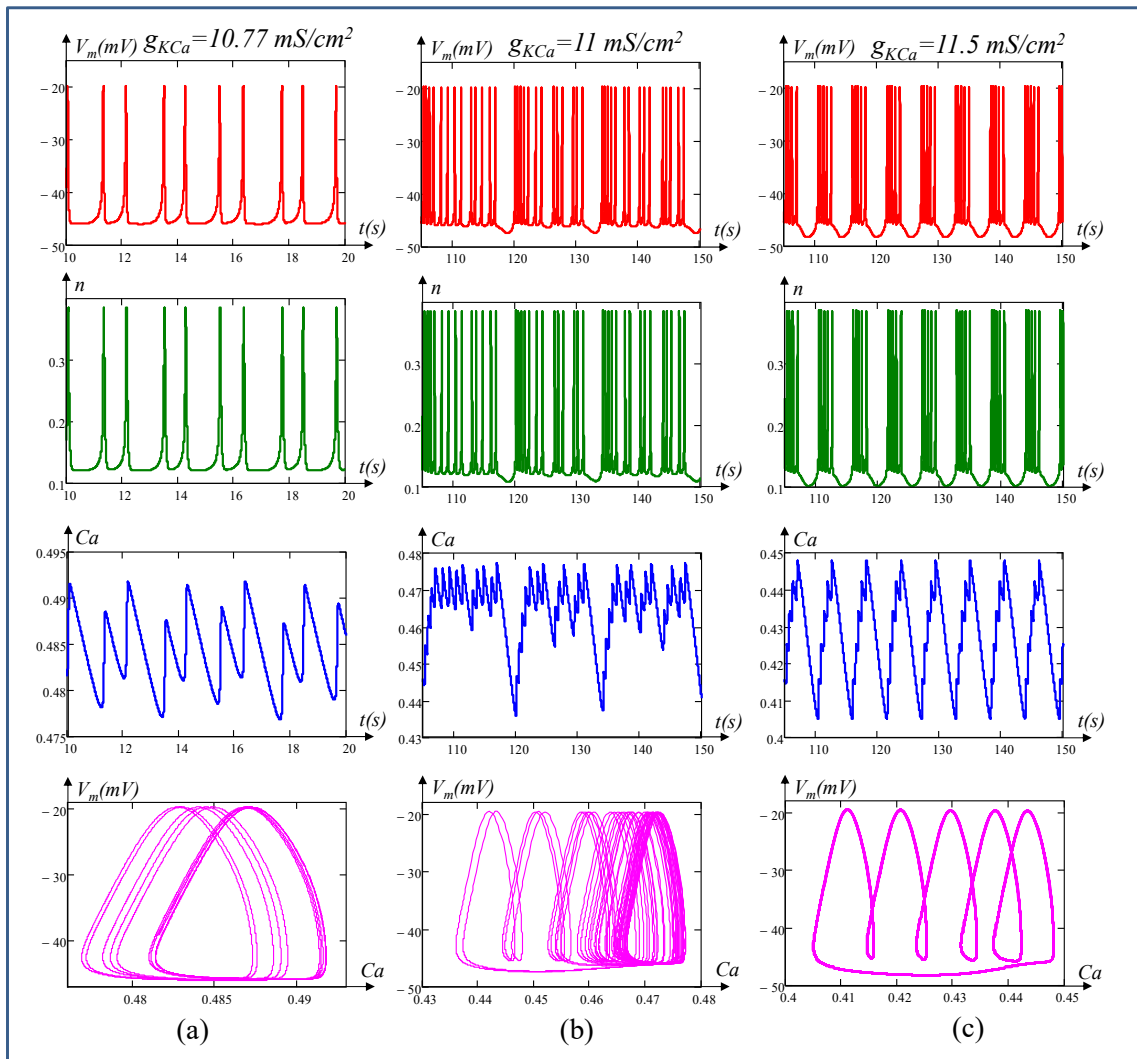


Figure 28. Different patterns of oscillations when g_{KCa} varied from 10.77 mS/cm^2 to 11.5 mS/cm^2 at DC stimulus current $I = 0$. (a) Period-8 oscillation at $g_{K,Ca} = 10.77 \text{ mS/cm}^2$; (b) Aperiodic (chaotic) oscillation at $g_{K,Ca} = 11 \text{ mS/cm}^2$; (c) Bursting at $g_{K,Ca} = 11.5 \text{ mS/cm}^2$. The simulations were performed at the initial conditions $V_m(0) = -50 \text{ mV}$, $n(0) = 0.1$, and $Ca(0) = 0.48$.

7. Concluding Remarks

This paper has provided a comprehensive and quantitative analysis of a biological excitable cell using the Chay neuron model. Through memristive theory, we have demonstrated that the voltage-sensitive mixed ion channel functions as a nonlinear resistor, while the voltage-sensitive potassium ion channel and calcium-sensitive potassium ion channel in an excitable cell are indeed time-invariant first-order generic memristors.

Furthermore, we have conducted in-depth analyses to derive the small signal model, admittance function, pole-zero diagrams, frequency response of admittance functions, and Nyquist plot at the DC equilibrium point Q. Our investigations revealed the existence of the local activity regime in the memristive Chay model within the voltage range of -49.455 mV to -24.685 mV and identified edge of chaos regime domains 1 and 2 within the voltage ranges of -49.455 mV to -48.763 mV and -27.984 mV to -24.685 mV , respectively. Moreover, consistent with the predictions of the Hopf bifurcation theorem, we observed the presence of an oscillating regime between two bifurcation points within the voltage range of -48.763 mV to -27.984 mV . Our numerical simulations confirmed the super-critical Hopf bifurcation with complex conjugates of eigen values coincident on the purely imaginary axis at $\pm 0.557i$ and $\pm 85.606i$, respectively. It was also observed that a tiny change in external stimulus current

I in excitable cells, far from the bifurcation points, no longer holds the Hopf bifurcation theorem as it crosses the imaginary axis from right to left, confirming that the real part of the eigen values becomes negative and converges to a DC equilibrium point.

Our comprehensive comparison of the HH, FitzHugh–Nagumo, ML, and Chay models presented in Table 2 along with their individual strengths and limitations revealed distinct advantages and drawbacks, making them suitable for different research contexts and questions. The selection of a particular model depends on the specific objectives. We primarily focused on advancing the understanding of excitable cells by modeling the networks of memristors and predicting their responses with the concepts of memristor theory, DC steady state analyses, small signal equivalent circuits, local activity principles, the edge of chaos theorem, and Hopf bifurcations. In conclusion, the theoretical framework outlined in this paper confirms the significance of memristors in simulating action potentials in excitable cells and also establishes a foundation for their application in neuron modeling, artificial intelligence, and brain-like machine interfaces. Our proposed model offers potential for enhancing adaptive neural networks, neuroprosthetics, neuromorphic computing architectures, and the broader scope of artificial intelligence, thereby aiding in the development of brain-like information processing systems.

Author Contributions: Conceptualization, M.S.; methodology, M.S.; software, M.S.; validation, M.S., A.A., V.R. and R.K.B.; formal analysis, M.S., A.A., R.T., V.R. and R.K.B.; investigation, M.S., A.A., R.T., V.R. and R.K.B.; writing—original draft preparation, M.S.; writing—review and editing, M.S., A.A., R.T., V.R. and R.K.B.; supervision, R.T. All authors have read and agreed to the published version of the manuscript.

Funding: This research received no external funding.

Data Availability Statement: The original contributions presented in the study are included in the article, further inquiries can be directed to the corresponding authors.

Conflicts of Interest: The authors declare no conflicts of interest.

Appendix A Abbreviations of the Model Parameters

| | |
|-------------|---|
| C_m | Membrane Capacitance |
| E_K | Potential across K^+ ion channel memristor |
| E_I | Potential across mixed ion channel memristor |
| E_L | Potential across leakage channel |
| E_{Ca} | Potential across Ca^{2+} ion channel memristor |
| $g_{K,V}$ | Voltage-sensitive K^+ ion-channel conductance |
| g_I | Voltage-sensitive mixed ion channel conductance |
| g_L | Leakage channel conductance |
| g_{KCa} | Calcium activated potassium conductance |
| k_{Ca} | Rate constant for the efflux of the intracellular Ca^{2+} ions |
| ρ | Proportionality constant |
| λ_n | Rate constant for K^+ ion-channel opening |
| m_∞ | Probability of activation of the mixed ion channel in steady state |
| α_m | The rate at which the activation of the mixed ion channel closed gates transition to an open state (s^{-1}) |
| β_m | The rate at which the activation of the mixed ion channel open gates transition to the close state (s^{-1}) |
| h_∞ | Probability of inactivation of the mixed ion channel in steady state |
| α_h | The rate at which the inactivation of the mixed ion channel closed gates transition to an open state (s^{-1}) |
| β_h | The rate at which the inactivation of the mixed ion channel open gates transition to the close state (s^{-1}) |
| n | Probability of n opening of the K^+ ion channel memristor |
| n_∞ | Steady state value of n |
| α_n | The rate at which K^+ ion channel closed gates transition to an open state (s^{-1}) |
| β_n | The rate at which K^+ ion channel opened gates transition to an close state (s^{-1}) |

References

1. Hodgkin, A.L.; Huxley, A.F. A quantitative description of membrane current and its application to conduction and excitation in nerve. *J. Physiol.* **1952**, *117*, 500–544. [[CrossRef](#)] [[PubMed](#)]
2. Chua, L.O.; Kang, S.M. Memristive devices and systems. *Proc. IEEE* **1976**, *64*, 209–223. [[CrossRef](#)]
3. Chua, L.O.; Sbitnev, V.I.; Kim, H. Hodgkin-Huxley axon is made of memristors. *Int. J. Bifurc. Chaos* **2012**, *22*, 1230011. [[CrossRef](#)]
4. Chua, L.O.; Sbitnev, V.I.; Kim, H. Neurons are poised near the edge of chaos. *Int. J. Bifurc. Chaos* **2012**, *22*, 1250098. [[CrossRef](#)]
5. Chua, L. Hodgkin-Huxley equations implies Edge of chaos kernel. *Jpn. J. Appl. Phys.* **2022**, *61*, SM0805. [[CrossRef](#)]
6. Chua, L. Everything you wish to know about memristor but are afraid to ask. *Radioengineering* **2015**, *24*, 319–368. [[CrossRef](#)]
7. Hodgkin, A.L.; Keynes, R.D. Experiments on the injection of substances into squid giant axons by means of microsyringe. *J. Physiol.* **1956**, *131*, 592–616. [[CrossRef](#)] [[PubMed](#)]
8. Morris, C.; Lecar, H. Voltage oscillations in the Barnacle giant muscle fiber. *J. Biophys. Soc.* **1981**, *35*, 193–213. [[CrossRef](#)] [[PubMed](#)]
9. Sah, M.P.; Kim, H.; Eroglu, A.; Chua, L. Memristive model of the Barnacle giant muscle fibers. *Int. J. Bifurc. Chaos* **2016**, *26*, 1630001. [[CrossRef](#)]
10. Rajamani, V.; Sah, M.P.; Mannan, Z.I.; Kim, H.; Chua, L. Third-order memristive Morris-Lecar model of barnacle muscle fiber. *Int. J. Bifurc. Chaos* **2017**, *27*, 1730015. [[CrossRef](#)]
11. Noble, D. A modification of the Hodgkin-Huxley equations applicable to Purkinje fibre action and pacemaker potentials. *J. Physiol.* **1962**, *160*, 317–352. [[CrossRef](#)] [[PubMed](#)]
12. Hudspeth, A.J.; Lewis, R.S. A model for electrical resonance and frequency tuning in saccular hair cells of the bull-frog *Rana catesbeiana*. *J. Physiol.* **1988**, *400*, 275–297. [[CrossRef](#)] [[PubMed](#)]
13. Giguère, C.; Woodland, P.C. A computational model of the auditory periphery for speech and hearing research. *J. Acoust. Soc. Am.* **1994**, *95*, 331–342. [[CrossRef](#)] [[PubMed](#)]
14. Nawrocki, R.A.; Voyles, R.M.; Shaheen, S.E. A mini review of neuromorphic architectures and implementations. *IEEE Trans. Electron. Devices* **2016**, *63*, 3819–3829. [[CrossRef](#)]
15. Lee, Y.; Lee, T.W. Organic synapses for neuromorphic electronics: From brain inspired computing to sensorimotor neurotronics. *Am. Chem. Soc.* **2019**, *52*, 964–974. [[CrossRef](#)]
16. Gentili, P.L. Photochromic and luminescent materials for the development of chemical artificial intelligence. *Dye. Pigment.* **2022**, *205*, 110547. [[CrossRef](#)]
17. Peercy, B.E.; Sherman, A.S. How pancreatic beta-cells distinguish long- and short-time scale CAMP signals. *Biophys. J.* **2010**, *99*, 398–406. [[CrossRef](#)]
18. Pedersen, M.G. Contributions of mathematical modeling of Beta-cells to the understanding of beta-cell oscillations and insulin secretion. *Diabetes Technol. Soc.* **2009**, *3*, 12–20. [[CrossRef](#)]
19. Felix-Martinez, G.J.; Godlinez-Fernandez, J.R. Mathematical models of electrical activity of the pancreatic β -cell. *Islets* **2014**, *6*, e949195. [[CrossRef](#)]
20. Kaestner, K.H.; Thompson, M.C.; Dor, Y.; Gill, R.G.; Glaser, B.; Kim, S.K.; Sander, M.; Stabler, C.; Stewart, A.F.; Powers, A.C. What is a β -cell? -Chapter I in the Human Islet Research Network (HIRN) review series. *Mol. Metab.* **2021**, *53*, 101323.
21. Lenzen, S. The pancreatic beta cell: An intricate relation between anatomical structure, the signalling mechanism of glucose-induced insulin secretion, the low antioxidative defence, the high vulnerability and sensitivity to diabetic stress. *ChemTexts* **2021**, *7*, 13. [[CrossRef](#)]
22. Marinelli, I.; Thompson, B.M.; Parekh, V.S.; Fletcher, P.A.; Gerardo-Giorda, L.; Sherman, A.S.; Satin, L.S.; Bertram, R. Oscillations in K(ATP) conductance drive slow calcium oscillations in pancreatic β -cells. *Biophys. J.* **2022**, *121*, 1449–1464. [[CrossRef](#)]
23. Marinelli, I.; Parekh, V.; Fletcher, P.; Thompson, B.; Ren, J.; Tang, X.; Saunders, T.L.; Ha, J.; Sherman, A.; Bertram, R.; et al. Slow oscillations persist in pancreatic beta cells lacking phosphofructokinase M. *Biophys. J.* **2022**, *121*, 692–704. [[CrossRef](#)] [[PubMed](#)]
24. Mukai, E.; Fujimoto, S.; Inagaki, N. Role of Reactive Oxygen Species in Glucose Metabolism Disorder in Diabetic Pancreatic β -Cells. *Biomolecules* **2022**, *2022*, 12091228. [[CrossRef](#)] [[PubMed](#)]
25. Millette, K.; Rodriguez, K.; Sheng, X.; Finley, S.D.; Georgia, S. Exogenous Lactogenic Signaling Stimulates Beta Cell Replication In Vivo and In Vitro. *Biomolecules* **2022**, *12*, 215. [[CrossRef](#)]
26. Bertram, R.; Marinelli, I.; Fletcher, P.A.; Satin, L.S.; Sherman, A.S. Deconstructing the integrated oscillator model for pancreatic β -cells. *Math. Biosci.* **2023**, *365*, 109085. [[CrossRef](#)]
27. Plant, R.E. Bifurcation and resonance in a model for bursting nerve cells. *J. Math. Biol.* **1981**, *11*, 15–32. [[CrossRef](#)]
28. Chay, T.R. Eyring rate theory in excitable membranes. Application to neural oscillations. *J. Phys. Chem.* **1983**, *87*, 2935–2940.
29. Chay, T.R.; Keizer, J. Minimal model for membrane oscillations in the pancreatic β -cell. *J. Biophys. Soc.* **1983**, *42*, 181–190. [[CrossRef](#)]
30. Chay, T.R. Chaos in a three-variable model of an excitable cell. *Physica D* **1985**, *16*, 233–242. [[CrossRef](#)]
31. FitzHugh, R. Impulses and physiological states in theoretical models of nerve membrane. *Biophys. J.* **1961**, *1*, 445–466. [[CrossRef](#)] [[PubMed](#)]
32. Chua, L. Five non-volatile memristor enigmas solved. *Appl. Phys. A Mater. Sci. Process.* **2018**, *124*, 563. [[CrossRef](#)]
33. Chua, L. If it's pinched it's a memristor. *Semicond. Sci. Technol.* **2014**, *29*, 104001. [[CrossRef](#)]
34. Chua, L.O.; Desoer, C.A.; Kuh, E.S. *Linear and Nonlinear Circuits*; McGraw-Hill Book Co.: New York, NY, USA, 1987.
35. Chua, L.O. *CNN: A Paradigm for Complexity*; World Scientific: Singapore, 1998.
36. Chua, L.O. Local activity is the origin of complexity. *Int. J. Bifurc. Chaos* **2005**, *15*, 3435–3456. [[CrossRef](#)]

37. Chua, L.O. Local activity principle: Chua's riddle, "Turing machine, and universal computing rule 137". In *The Chua Lectures: From Memristors and Cellular Nonlinear Networks to the Edge of Chaos*; World Scientific Series on Nonlinear Science; World Scientific: Singapore, 2020.
38. Ascoli, A.; Demirkol, A.S.; Chua, L.O.; Tetzlaff, R. Edge of chaos theory resolves Smale paradox. *IEEE Trans. Circuit Syst. I* **2022**, *69*, 1252–1265. [[CrossRef](#)]
39. Sah, M.P.; Mannan, Z.I.; Kim, H.; Chua, L. Oscillator made of only One memristor and one battery. *Int. J. Bifurc. Chaos* **2015**, *25*, 1530010. [[CrossRef](#)]
40. Ascoli, A.; Demirkol, A.S.; Chua, L.O.; Tetzlaff, R. Edge of chaos is sine qua non for Turing instability. *IEEE Trans. Circuit Syst. I* **2022**, *69*, 4596–4609. [[CrossRef](#)]
41. Ascoli, A.; Demirkol, A.S.; Chua, L.O.; Tetzlaff, R. Edge of chaos explains prigogine's instability of the homogeneous. *IEEE J. Emerg. Sel. Top. Circuits Syst. (JETCAS)* **2022**, *12*, 804–820. [[CrossRef](#)]
42. Ascoli, A.; Demirkol, A.S.; Tetzlaff, R.; Chua, L.O. Analysis and design of bio-inspired circuits with locally-active memristors. *IEEE Trans. Circuit Syst. II* **2024**, *71*, 1721–1726. [[CrossRef](#)]
43. Ascoli, A.; Demirkol, A.S.; Tetzlaff, R.; Chua, L.O. Edge of chaos theory sheds light into the all-or-none phenomenon in neurons—Part I: On the fundamental role of the sodium ion channel. *IEEE Trans. Circuit Syst. I* **2024**, *71*, 5–19. [[CrossRef](#)]
44. Ascoli, A.; Demirkol, A.S.; Tetzlaff, R.; Chua, L.O. Edge of chaos theory sheds light into the all-or-none phenomenon in neurons—Part II: On the necessary and sufficient conditions for the observation of the entire life cycle of an action potential. *IEEE Trans. Circuit Syst. I*, **2023**; *under review*.

Disclaimer/Publisher's Note: The statements, opinions and data contained in all publications are solely those of the individual author(s) and contributor(s) and not of MDPI and/or the editor(s). MDPI and/or the editor(s) disclaim responsibility for any injury to people or property resulting from any ideas, methods, instructions or products referred to in the content.